Astronomy & Astrophysics manuscript no. output
June 20, 2022

MINCE I. Presentation of the project and the first sample ⋆

1

Received September 15, 1996; accepted March 16, 1997

ABSTRACT

Context. In recent years, Galactic Archaeology is a vibrating field of Astronomy . Its main focus are the oldest stars of our Galaxy, in most cases identified as the most metal-poor stars. However, the struggle for finding these ancient fossils has produced an important bias in the observations, in particular the intermediate metal poor stars (−2.5<[Fe/H]< −1.5) have been frequently overlooked. The missing information has consequences for the precise study of the chemical enrichment of our Galaxy in particular for what concerns neutron capture elements and it will be only partially covered by future multi object spectrograph surveys such as WEAVE and 4MOST.
Aims. Measuring at Intermediate Metallicity Neutron Capture Elements (MINCE) is gathering high quality spectra (high signal to noise and high resolution) of several hundreds bright stars and metal poor stars , manly from of our Galactic halo. In this paper we present the first sample of 42 stellar spectra for 40 different stars with the abundances of the elements up to the iron peak.
Methods. We describe the selection we have used which is manly relying on *Gaia* data. We present also the way we determine the stellar atmospheres of our sample and the chemical abundances in each star.
Results. We obtain $T_{\rm eff}$, log g, micro turbulence and metallicity ([Fe/H]) for all the 42 stellar spectra. Eight targets are not in the optimal metallicity range for MINCE; for the remaining 34 stellar spectra, we determine the chemical abundances of 19 elements from oxygen to zinc based on synthetic spectra in local thermodynamic equilibrium. **For all the 40 stars, we also calculate the kinematical properties and we found that 8 stars belong to the thin disc, 15 to disrupted satellites and the remaining cannot be associated to the mentioned structures, and we call them halo stars.** We also show the chemical evolution results for eleven chemical elements, based on recent models.
Conclusions.
Spectra taken from different spectrographs produce quite consistent results and the chemical abundances derived for the MINCE sample are in agreement with previous results obtained in literature, therefore we can adopt this method for the rest of our sample. The future steps in the project are to apply the method described here to the larger sample we have gathered in the recent period and prepare a similar method to be applied to the careful determination of the neutron capture elements from our spectra

Key words. Stars: abundances - Galaxy: abundances - Galaxy: evolution - Galaxy: formation -

1. Introduction

The project MINCE (Measuring at Intermediate metallicity Neutron-Capture Elements) aims to gather abundances for neutron-capture elements of several hundreds stars at intermediate metallicity using different facilities worldwide. The idea is to study the nucleosynthetic signatures that can be found in old stars, in particular in the specific class of chemical elements with Z > 30, i.e. the neutron-capture elements. They are mainly formed through multiple neutron captures, and not through the fusion reaction that create the fast majority of element up to the iron peak. The neutron-capture process is split in the rapid process (r-process) or slow process (s-process) depending on whether the timescale for neutron capture is faster or slower than radioactive beta decay, according to the initial definition by Burbidge et al. (1957). These elements have complex nucleosynthesis and they are not yet deeply investigated as - e.g. $\alpha-$elements. The most recent investigation expanded the number of stars with detailed chemistry at extremely low metallicity up to approximately a thousand objects (e.g. Roederer et al. 2014; Yong et al. 2014). After this incredible effort in searching and measuring the most extreme metal-poor stars – that is still ongoing – it is natural to think that adding valuable knowledge in this field can be difficult or extremely expensive. However, the search for the lowest possible metallicity almost completely ignored all the stars in the intermediate range of metallicity between the very metal-poor stars ([Fe/H]< −2.5) and thin or thick disc stars ([Fe/H]> −1.5). In this region, the number of stars with any measurements of the neutron-capture elements is small, only 25% (332 objects) according to the sample gathered by the JINA database (1213), and less than 10% (103) with Eu measurements. According to the metallicity distribution function of the Galactic halo (Bonifacio et al. 2021a) there is a factor of 12 more halo stars in this region than at lower metallicity, therefore an enormous number of halo stars are yet unexplored as far as the abundances of neutron-capture elements go.

In this first paper, we present a first sample of 42 stellar spectra (40 unique stars). We present the atmospheric parameters measured for all the 42, but we carry out the detailed abundances determinations only of 34 (32 stars), eight stars being too metal rich for MINCE goals. The spectra of these stars were taken at four different facilities thanks to four accepted proposals and it clearly shows the joint efforts of the MINCE team. We also introduce how we have selected our MINCE stars and the issues that we have found in the search of an optimal selection of bright halo stars for our telescopes. Finally, we describe the approach we intend to assume for all the MINCE stars to determine the atmospheric parameters of the stars. For this first sample, the results of the chemical abundances cover the elements up to zinc. The actual measurement of the heavy neutron capture elements

⋆ Based on observations made with HARPSN at TNG, Fies at NOT, Sophie at OHP and Espadons at CFHT

will be tackled in the next MINCE paper. **We also investigated the kinematics of the stars in our sample making use of the Gaia astrometric parameters and the radial velocities (RV) we measured.** All the results obtained and published by MINCE will produce a catalogue of high-quality spectra with precise atmospheric parameters and chemical abundances constructed by combining observations from several facilities. All results will be made available at...

2. Selection

The stellar candidates were selected to be metal-poor ([M/H]< −0.7) and bright (V<10) giants ($T_{\rm eff}$ <5000 K) based on Starhorse (Anders et al. 2019). We named this method "mince1". Starhorse combines the precise parallaxes and optical photometry delivered by *Gaia*'s second data release with the photometric catalogues of Pan-STARRS1, 2MASS, and AllWISE and derived Bayesian stellar parameters, distances, and extinctions for 137 million stars. After the first night on TNG covering eight candidates, we found that the selection was not providing the requested metallicity range: the candidates were too metal rich for the MINCE goals. For this reason, we decide to add a constrain on the kinematics of the stars ($v_{\rm tot}$ > 200 km/s) to select halo stars, exploiting the precise measurements of *Gaia*. This selection scheme improved the success rate to almost 100%. We named this method "mince2". The eight stars mentioned above are not fully considered here, their metallicities being above the threshold we set for MINCE and we present only their atmospheric parameters; the analysis of their chemical abundances will be carried out in a forthcoming paper devoted to more metal rich stars compared to MINCE limits. The sample comprises relative bright objects and we set the observations to reach approximately a S/N ~ 100 at 500 nm see Table A.1-A.3. We also include in this first paper two stars that were actually selected from the Apache Point Observatory Galactic Evolution Experiment (APOGEE) survey (Eisenstein et al. 2011). With a higher resolution and different spectral coverage MINCE can provide different elements, and also a comparison with the results obtained by APOGEE in the infrared.

3. Observations and data reduction

As mentioned in the Introduction, this sample comprises spectra taken from several facilities and obtained thanks to a total of four proposals with three different Principle Investigators: Cescutti for HARPS-north at TNG, E. Spitoni for FIES at NOT and P. Bonifacio for Sophie at OHP and ESPaDOnS at CFHT. Details on the observations are provided in tables A.4 to A.7.

3.1. TNG HARPS-N

The 3.58m telescope Telescopio Nazionale Galileo (TNG), is the Italian facility located at the Roque de Los Muchachos Observatory in the Canary island of La Palma. We used HARPS-N (Cosentino et al. 2012), which is a high-resolution (resolving power R=115,000), high-stability visible (383-693 nm) spectrograph. Long-term stability allows an accuracy better than <1m/s in the radial velocity measurements and it is excellent for the discovery and characterization of exoplanets, but it is also well suited for stellar abundance spectroscopy. The spectra were taken in service mode in 2 nights in May and June 2020. For the reduction of the echelle spectra, we used the standard pipeline. The radial velocities are determined by the pipeline through cross-correlation with a mask appropriate for the spectral type of the star.

3.2. NOT FIES

The Nordic Optical Telescope (NOT) is a 2.56-m telescope also located at the Spanish Roque de los Muchachos Observatory, about 1km away from the TNG. We used FIES (Telting et al. 2014), a cross-dispersed high-resolution echelle spectrograph with a maximum spectral resolution of R = 67000. The entire spectral range 370-830 nm is covered without gaps in a single, fixed setting. Most of the spectra were taken in service mode during June 2020, see Table**??** for specific dates. Also in this case, we used the output of the standard pipeline, which are available upon request. Radial velocities are not provided by the pipeline. They have been determined by template matching (see e.g. **?**) over the range 400 nm to 660 nm. The template was a synthetic spectrum computed with the parameters provided in Table 1. The error provided in Table **??** is just based on the χ^2 of the fit and does not take into account systematic errors. The systematic errors due to the fact that the calibration arc was taken several hours before the observation can be of the order of a few 100 m/s (J. Telting, priv. comm.). The mid-exposure time was taken from the descriptor DATE-AVG in the FITS header of each observation. From this time, the barycentric julian date (BJD) and the barycentric correction were computed using the tools OSU Online Astronomy Utilities[1] that implement the methods and algorithms described in Wright & Eastman (2014).

3.3. OHP 1.93 Sophie

The OHP 1.93m telescope is located in at the Observatoire de Haute Provence, in southern France. The spectra were obtained with the Sophie spectrograph (Bouchy & Sophie Team 2006) at high-resolution mode, that providing a resolving power R=75 000 and a spectral range from 387.2 nm to 694.3 nm. The spectra were obtained in visitor mode, during three nights from August 24 to 26, 2020, the observer was P. Bonifacio. The wavelength calibration relied both on a Th-Ar lamp and on a Fabry-Pérot etalon. The data was reduced automatically on-the-fly by the Sophie pipeline. In a similar way as for HARPS-N the pipeline determines radial velocities from cross-correlation wit a suitable mask.

3.4. CFHT ESPaDOnS

The 3.6m Canada-France-Hawaii telescope (CFHT) is located on the summit of Mauna Kea, in the island of Hawai, USA. The spectra were obtained with the fibre-fed spectropolarimeter ESPaDOnS (Donati et al. 2006). The observation were obtained in the Queued Service Observation mode of CFHT in 2020. The spectroscopic mode “Star+Sky” was used, providing a resolving power of R=65 000 and the spectral range 370 nm to 1051 nm. The data was delivered to us reduced with the Upena[2] pipeline that uses the routines of the Libre-ESpRIT software (Donati et al. 1997). The output spectrum is provided in an order-by-order format, we merged the orders using an ESO-MIDAS[3] with a script written by ourselves. The pipeline applies the barycentric correction to the reduced spectrum and provides the Heliocentric Julian Date (HJD), we transformed this to BJD using the tool `https:`

[1] `https://astroutils.astronomy.osu.edu/`
[2] http://www.cfht.hawaii.edu/Instruments/Upena/
[3] https://www.eso.org/sci/software/esomidas/

//astroutils.astronomy.osu.edu/time/utc2bjd.html that implements the methods and algorithms described in Wright & Eastman (2014). The pipeline corrects the wavelength scale using the telluric absorption lines, this should compensate for the difference in temperature and pressure between the time when the calibration arc was taken and the time of the observation. Like for the FIES spectra we measured the radial velocities by template matching over the range 400 nm to 660 nm. We underline that the error provided in Table A.7 is based on the χ^2 of the fit, thus takes into account only the noise in the spectrum and not any systematic error. In spite of the fact that ESPaDOnS is protected by two thermal enclosures, its temperature and pressure are not actively controlled, like those of HARPS-N or Sophie. According to the documentationthe expected precision using the telluric correction is 20 ms^{-1}. For star TYC 3085-119-1 we have two spectra, but although the radial velocity was measured for both, the chemical analysis was performed only on the second spectrum that has S/N ~ 100 at 500 nm against ~ 60 for the first spectrum. The improvement in S/N by coadding the two spectra would be marginal.

3.5. Radial velocities

Our measured radial velocities are generally in very good agreement with the *Gaia* radial velocities. However there are eleven spectra, of ten stars for which the difference between our measurement and *Gaia* exceeds 3σ, where σ is computed by adding under quadrature the errors associated to each measurement. In some cases this is certainly due to real radial velocity variations and this can originate by the fact that the star is a binary system. In none of our spectra we detect a secondary spectrum of a companion, so if any of the stars is binary indeed, the companion must be much less luminous, implying a small veiling of the spectrum. This gives us confidence on our approach of analysing all stars as single stars.

The most clear case is TYC 4584-784-1 for which our Sophie radial velocity differ by 10.29 kms^{-1} from that of *Gaia*. Also the error on the *Gaia* radial velocity is large for a star of this brightness, almost 1 kms^{-1}. Other very clear cases are TYC 4331-136-1, BD –07 3523, BD +24 2817, HD 139423, BD +39 3309, HD 354750 and TYC 565-1564-1. A borderline case is that of TYC 2824-1963-1 two Sophie spectra provide radial velocities that differ by just over 3σ from that of *Gaia*, which however has a an error of only 0.33kms^{-1}. It will be interesting to see the *Gaia* DR3 radial velocity for this star.

A controversial case is that of BD +07 4625. For this star we have observed two spectra with FIES and one with Sophie. The Sophie radial velocity is at 4σ of the *Gaia* one, while the two FIES radial velocities are at 0.19 and 1.9 σ from the *Gaia* one, which has a small error of 0.19 kms^{-1}. The FIES spectra were taken 55.75 days before the Sophie one. One should also consider that the standard deviation of the FIES and Sophie radial velocities is of 0.48 kms and the mean is perfectly consistent with *Gaia*. Again the *Gaia* DR3 radial velocities for this star will be very interesting. Another suspicious case is BD +25 4520. This star has been observed with HARPS-N and 77 days later with Sophie. While the radial velocity derived from the HARPS-N agrees with the *Gaia* radial velocity to better than 1σ that from the Sophie spectrum differs by more than 3σ. It is interesting to note that the *Gaia* radial velocity has been derived from only three transits, and that the the *Gaia* error, 0.32 kms^{-1}, is very similar to the standard deviation of the two HARPS-N and SOPHIE measurements, 0.35 kms^{-1}. We suspect this star to be a radial velocity variable of low amplitude, possibly of the order of 1 kms^{-1}.

4. Analysis

4.1. Stellar parameters

The sample presented here is the the first of a series and we expect to have many spectra to be analyse in the future, as explained in Sec.2. We then need an a way to analyse these stars that is as automated and objective as possible The stellar parameters have been derived by using the *Gaia* data release early three (*Gaia* EDR3). To deredden the *Gaia* photometry, we used the maps from Schlafly et al. (2012), and by iterating the computation of the dereddening we took into account the stellar parameters. First, we derived the absolute G magnitude by applying the parallax, corrected for the zero point as suggested by Lindegren et al. (2021). The *Gaia* $G_{BP} - G_{RP}$ colour, the absolute G magnitude with a first guess metallicity have been compared to synthetic colours in order to derive the first guess stellar parameters. This first guess of the stellar parameters are fed to MyGIsFOS (Sbordone et al. 2014) to derive the stellar metallicity. The metallicity derived by MyGIsFOS is then used as input to derive new stellar parameters. The process has been iterated up to when the changes in stellar parameters were less than 50 K in $T_{\rm eff}$, and less than 0.05 dex in log g. For the micro-turbulence, we used the calibration by Mashonkina et al. (2017) at any iteration, and applied these values as final choice. The stellar parameters and derived metallicity are reported in Table 1.

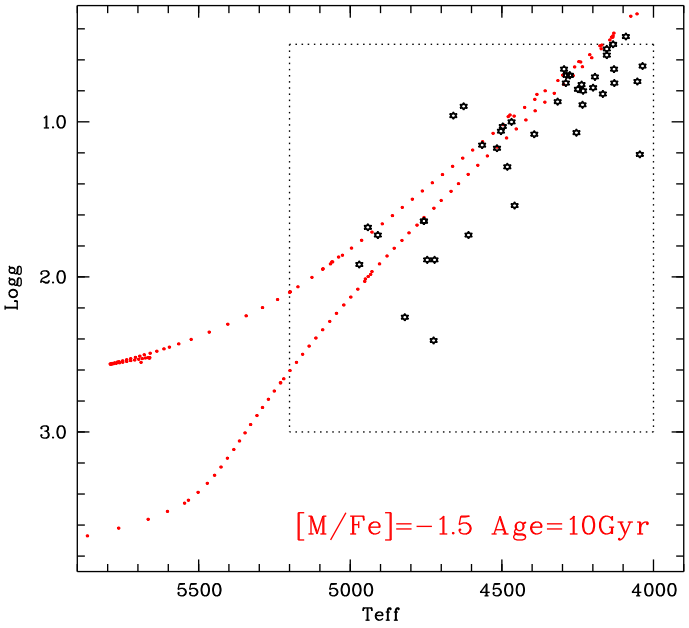

Fig. 1. The ($T_{\rm eff}$,log g) plot with the observed stars (black stars) and a PARSEC (Bressan et al. 2012; Marigo et al. 2017) isochrone of 10 Gyr and metallicity −1.5. The dashed lines delimit the grid used by MyGIsFOS in the chemical analysis. **LL: this figure is not mentioned in the text**

4.2. Comparison of the stellar parameters with Starhorse

The results obtained for the stellar parameters from our spectra can be compared to those obtained by Starhorse. This comparison can be important to evaluate the use of this database. In Fig.2, we show the case of log g where a positive offset (0.16

Table 1. Stellar parameters of the sample with extra information. For column "Selection" see Sect 2; columns parallax, g, and bp-rp are from *Gaia* (DR2), teff50 and log50 are from the Starhorse database (excluding * taken from APOGEE survey); vel_{tot} was computed from *Gaia* (DR2) data considering proper motions, parallax and radial velocity.

Star	$T_{\rm eff}$ [K]	log g [gcs]	ξ kms^{-1}	[Fe/H]	Selection	parallax mas	G mag	$G_{BP}-G_{RP}$ mag	teff50 [K]	logg50 [cgs]	vel_{tot} kms^{-1}
TYC 2588-1386-1	4130	0.66	1.99	-1.74	APOGEE	0.129	11.73	1.58	4319*	1.27*	289.0
TYC 3085-119-1	4820	2.26	1.56	-1.51	APOGEE	0.954	10.38	1.12	4745*	2.14*	122.0
BD+13 2383	4458	1.54	1.65	-0.56	mince1	1.319	8.54	1.35	4751	1.68	27.0
BD+24 2817	4722	1.89	1.56	0.02	mince1	1.61	8.54	1.3	4981	2.12	73.0
BD-00 3963	4970	1.92	1.68	-0.13	mince1	1.68	8.54	1.3	4936	2.0	43.0
HD 87740	4746	1.89	1.62	-0.56	mince1	1.448	8.56	1.2	4838	1.96	45.0
HD 91276	4610	1.73	1.63	-0.58	mince1	1.372	8.57	1.26	4802	1.83	60.0
HD 130971	4045	1.21	1.61	-0.64	mince1	1.247	8.6	1.68	4658	1.48	40.0
HD 138934	4725	2.41	1.34	-0.19	mince1	2.296	8.01	1.26	4947	2.12	27.0
HD 165400	4942	1.68	1.79	-0.25	mince1	1.37	8.34	1.27	4825	1.78	23.0
BD+03 4904	4497	1.03	2.06	-2.58	mince2	0.398	9.5	1.38	4528	1.1	307.0
BD+04 18	4053	0.74	1.9	-1.48	mince2	0.293	9.19	1.6	4284	0.67	484.0
BD+06 2880	4167	0.82	1.91	-1.45	mince2	0.616	9.18	1.53	4463	1.14	378.0
BD+07 4625	4757	1.64	1.86	-1.93	mince2	1.209	8.61	1.24	4877	1.79	570.0
BD+07 4625	4757	1.64	1.86	-1.95	mince2	1.209	8.61	1.24	4877	1.79	570.0
BD+11 2896	4254	1.07	1.83	-1.41	mince2	0.771	8.72	1.48	4243	1.21	286.0
BD+20 3298	4154	0.57	2.07	-1.95	mince2	0.476	8.77	1.64	4742	1.39	423.0
BD+25 4520	4276	0.7	2.08	-2.27	mince2	0.245	9.25	1.61	4386	0.72	445.0
BD+25 4520	4276	0.7	2.08	-2.28	mince2	0.245	9.25	1.61	4386	0.72	445.0
BD+31 2143	4565	1.15	2.03	-2.37	mince2	0.595	8.87	1.3	4689	1.26	359.0
BD+32 2483	4516	1.17	1.99	-2.25	mince2	0.404	9.83	1.32	4473	1.3	259.0
BD+35 4847	4237	0.76	2.01	-1.92	mince2	0.644	8.46	1.61	4725	1.48	263.0
BD+39 3309	4909	1.73	1.94	-2.58	mince2	0.704	9.6	1.1	4855	1.9	300.0
BD+48 2167	4468	1.0	2.04	-2.29	mince2	0.429	9.32	1.36	4498	1.09	255.0
BD-00 4538	4482	1.29	1.88	-1.9	mince2	0.853	8.77	1.34	4607	1.41	320.0
BD-07 3523	4193	0.71	2.02	-1.95	mince2	0.408	9.12	1.58	4410	0.83	249.0
HD 115575	4393	1.08	1.94	-1.99	mince2	0.694	9.02	1.45	4579	1.26	324.0
HD 139423	4287	0.7	2.05	-1.71	mince2	0.808	8.02	1.5	4369	0.92	431.0
HD 142614	4316	0.87	1.96	-1.46	mince2	0.668	8.73	1.45	4370	1.12	412.0
HD 208316	4249	0.79	1.98	-1.61	mince2	0.654	8.35	1.51	4390	0.9	315.0
HD 238439	4154	0.53	2.1	-2.09	mince2	0.29	9.26	1.6	4533	0.96	415.0
HD 354750	4626	0.9	2.17	-2.36	mince2	0.177	10.59	1.43	4426	0.94	235.0
TYC 4-369-1	4234	0.89	1.94	-1.84	mince2	0.216	10.78	1.49	4439	0.96	345.0
TYC 33-446-1	4289	0.75	2.07	-2.22	mince2	0.185	10.09	1.52	4323	0.69	280.0
TYC 1008-1200-1	4199	0.78	2.01	-2.23	mince2	0.226	10.19	1.74	4335	0.7	426.0
TYC 2824-1963-1	4036	0.64	1.95	-1.6	mince2	0.185	10.06	1.69	4241	0.66	433.0
TYC 3944-698-1	4091	0.45	2.11	-2.18	mince2	0.225	9.9	1.81	4523	0.96	270.0
TYC 4001-1161-1	4129	0.75	1.94	-1.62	mince2	0.42	10.09	1.87	4556	1.07	423.0
TYC 4221-640-1	4295	0.66	2.12	-2.27	mince2	0.188	10.59	1.55	4421	0.82	387.0
TYC 4267-2023-1	4660	0.96	2.11	-1.74	mince2	0.62	9.5	1.84	4607	1.16	372.0
TYC 4331-136-1	4133	0.5	2.13	-2.53	mince2	0.513	9.53	2.11	4385	0.74	201.0
TYC 4584-784-1	4232	0.8	2.0	-2.04	mince2	0.192	10.62	1.59	4261	0.78	326.0
BD+21 4759	4503	1.06	2.05	-2.51	mince2	0.397	9.44	1.37	4565	1.15	266.0

dex) and a dispersion are visible, in particular for log g<1, with a standard deviation of 0.20 dex. In Fig. 3, we present the case of $T_{\rm eff}$. Again there is a positive offset of 154 K, with a standard deviation of 176 K most prominent for $T_{\rm eff}$<4300 K. Overall, the Starhorse database is certainly suitable for our selection, at least for what concern log g and $T_{\rm eff}$. In the future, we will also consider to use the values derived by Starhorse as first guess of the stellar parameters applying suitable corrections inferred by the comparison with our results, omitting the procedure described above. In both figures, we present also the comparison to the measurements obtained by the APOGEE survey, although only for a sample of two stars. We cannot draw valid conclusions from only two objects, but clearly for the cooler star the difference in log g is not negligible, although the $T_{\rm eff}$ shows only a moderate difference of $\sim$ 200 K.

4.3. Kinematics

We investigated the kinematics of the stars in our sample making use of the Gaia astrometric parameters and the radial velocities (RV) we measured. In particular, for the RVs we adopted weighted means for stars having SOPHIE, HARPS-N, ESPADONS and Gaia values. In the case of ESPADONS RVs we adopted an error on the RV of 20 m/s. For stars having FIES and Gaia measures or with measures more than 3 σ different from the

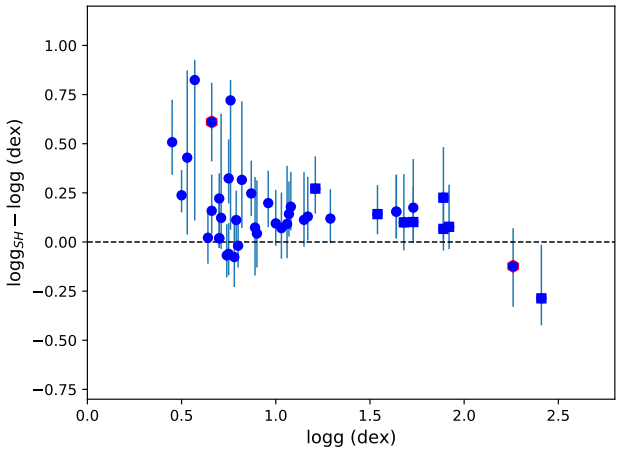

Fig. 2. The comparison of the log g obtained for our MINCE stars to the log g obtained by Starhorse Anders et al. (2019), the blue solid dots are the stars selected with the mince2 selection, the squares with mince1. The error-bars considered are 84th and 16th percentile obtained from the Bayesian approach used in Starhorse. There are two exceptions, presented with hexagons with a red contour These two stars were selected from the APOGEE survey, from which we adopted the comparison log g and the errors.

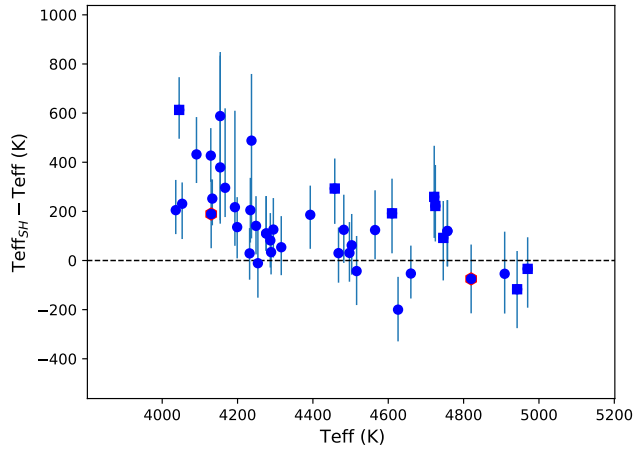

Fig. 3. The same as Fig.2, but for the $T_{\rm eff}$.

Gaia values, we adopted the non-weighted means of the values available.

In order to evaluate kinematic quantities and the actions, we used the `galpy` code (Bovy 2015) together with the MWPotential14 potential and the solar motion of Schönrich et al. (2010). We adopted a solar distance from the galactic centre of 8 kpc and a circular velocity at the solar distance of 220 kms^{-1} (Bovy et al. 2012).

Following Bonifacio et al. (2021b), we evaluated the corresponding errors using the `pyia` code. For each stars, we extracted 1000 instances of the input parameters (coordinates, proper motions, distance and radial velocity) from a multivariate Gaussian which takes into account the covariance matrix. Each instance is then fed to `galpy`. For each parameter calculated, we adopt as errors the standard deviations of the 1000 realizations. Notice that the quantities reported in Tables 2 and 3 are the value obtained from the input parameters taken at face value, only the reported errors are evaluated with the procedure described above.

In Figure 4, we present our targets (black filled symbols) in a few planes commonly used to characterize the stellar kinematic. For reference, we plot in gray in each panel the "good-parallax" sample from Bonifacio et al. (2021b).

Considering Galactocentric cylindrical coordinates, in the top-left panel we present the component of the velocity in the plane of the Galaxy (V_T) *vs* a combination of the radial and vertical component of the velocity ($\sqrt{V_R^2 + V_Z^2}$), namely a version of the Toomre diagram. In this plane, disc stars are visible as the roughly circular concentration of stars in the bottom-right of the figure. Stars in prograde motions are found at V_T >0.

The top-right panel shows the relation between two integrals of motion, namely the orbital energy per unit mass E *vs* the vertical component of the angular momentum L_Z. In this plane disc stars are found as a concentration in the middle right part of the figure. Stars in prograde motions are found at L_Z >0.

The bottom-right panel shows the so-called action diamond, namely the difference between the vertical and radial actions (J_Z-J_R) *vs* the azimuthal action (J_ϕ = L_Z), normalized to J_{tot} = $|J_\phi|$+J_Z+J_R. In this plane, disc stars are found in the middle-right corner of the figure.

Finally, the bottom-left panel presents the square root of the radial action $\sqrt{J_R}$ *vs* the azimuthal action J_ϕ. Disc stars are visible at the bottom right of the figure.

The two bottom panels were used by Feuillet et al. (2021) to select candidates likely belonging to the *Gaia*-Sausage-Enceladus (GSE, Belokurov et al. 2018; Haywood et al. 2018; Helmi et al. 2018) and the Sequoia (Barbá et al. 2019; Villanova et al. 2019; Myeong et al. 2019) accretion events. The selection box they used for GSE and Sequoia (red and green shaded areas in the left and right panels) are indicated. Stars in the background populations following in these two selections box are reported in red (GSE candidates) and green (Sequoia candidates) in the upper panels.

GSE candidates are highly eccentric (large $\sqrt{J_R}$ values) and do not have a large angular momentum (small values of J_ϕ = L_Z). Sequoia candidates are highly retrograde (highly negative values of J_ϕ = L_Z) and their orbits are not as eccentric as those of GSE candidates.

Among the stars in our sample, we identify 12 and 3 stars with kinematics compatible with the GSE (black filled diamond) and Sequoia (black filled squares) structures, respectively, according to the selections boxes of Fig. 4. We identify them in Tables 2 and 3. We also identify 8 stars with thin disc kinematics (black filled triangles). These are the most metal-rich stars in the sample ([Fe/H]>-0.7 dex) and are confined to the disc (Z<0.8kpc and Z_{max}<0.9kpc). One star likely belong to the thick disc (TYC 3085-119-1, filled blue circle at V_T=+140 kms^{-1}in the top-left panel; [Fe/H]=-1.5, e=0.36, Z=0.6 kpc, Z_{max}=1.6 kpc). The remaining stars (filled blue circles) may be associated with the halo and have in roughly equal number prograde and retrograde orbits. They are formally not associated with GSE or Sequoia, although some of them lie quite close to GSE or Sequoia stars in the various planes.

Shall we use the classification scheme of Bensby et al. (2014), besides TYC 3085-119-1, also stars HD143348 and HD354750 would be classified as thick disc stars while the classification of the remaining stars as belonging to the thin disc or the halo would be confirmed. As expected, candidate GSE and Sequoia stars would be classified as halo stars. HD143348 and HD354750 are indeed confined to the disc (Z_{max}=1.19 and 2.51

kpc, respectively). They have, however, highly eccentric orbits (ecc.=0.62 and 0.87, respectively).

5. Abundances

With MyGIsFOS we derived the abundances up to the iron peak, that we report in the Tables A.1- A.3, where we also provide the errors based on standard deviation of the abundances measured from the different lines of the same ion: for this reason, ions measured from a single line do not have associated errors. It is realistic to consider in this case the highest sigma obtained among the other elements. Moreover, to these errors, one should add in quadrature the error generated from the assumed stellar atmospheres. Typical errors due to uncertainties in atmospheric parameters are the same as provided in Table 8 of Matas Pinto et al. (????). The two stars in that paper are in the typical parameter range of the MINCE targets and have been analysed with the same methods. When not specified, we adopt as metallicity the abundance derived from Fe I lines. **PB check the following is true!** Since our surface gravities are derived form the parallaxes and not Fe ionisation equilibrium, in order to minimise the gravity dependence in abundance ratios we adopt [X/Fe] = [X/Fe I] where X is a neutral species and [X/Fe] = [X/Fe II] for ionised species. The exception is oxygen: since all our oxygen abundances are derived from the forbidden lines, whose dependence on surface gravity is closer to that of an ionised species than to that of a neutral species we adopt [O/Fe] = [O/Fe II] as done by Cayrel et al. (2004). The solar abundances we adopted are reported in Table 5 and they are the values we used to computed our stellar models as well as to derive [X/H] and [X/Fe] ratios.

5.1. Sulphur abundances

A different method was adopted to derive the abundances of sulphur; the S I lines of Multiplet 1 at 920 nm and Multiplet 6 at 860 nm lie in the wavelengths ranges covered only by the spectra taken at CFHT with the spectrograph ESPaDOnS. While we considered the lines at 920 nm, we discarded those at 860 nm because too weak to be measured. The features of Multiplet 1 are among the strongest lines of Sulphur (S) but they are located in a wavelength range contaminated by telluric lines. To assess the suitability of Mult. 1 lines for the estimation of sulphur abundances, we compared the observed spectrum of stars with that of a B-type star. Sulphur lines contaminated by telluric ones were rejected, while we measured the sulphur abundances from not contaminated lines by spectrosynthesis. We used the code SALVADOR (Mucciarelli in prep.) that computes a grid of synthetic spectra with the code SYNTHE (Kurucz 1993b, 2005), using ATLAS9 α-enhanced model atmospheres (Kurucz 1993a) based on ODF by **?**. SALVADOR finds the abundance from a line performing a χ^2 minimisation between observed and synthetic spectra. In the cases where Multiplet 1 lines were blended with telluric ones, we estimated the abundances from equivalent width (EW). Exploiting the deblending option of the IRAF task splot, we taken into account the contribution of telluric lines and we measured the EW of S lines. The measured EW were converted in abundances using the code GALA Mucciarelli et al. (2013). The results obtained are listed in Table 4. We reported also the the abundances corrected for deviations from local thermodynamic equilibrium (LTE). The non-LTE corrections were assumed following Takeda et al. (2005) and we found a mean correction of $\Delta \sim -0.25$. The [S/Fe] values were obtained considering the solar value $[S/Fe]_{\odot}$=7.16 (Caffau et al. 2014).

6. Reference chemical evolution models

The main scope of Galactic Archaeology is to constrain the formation and evolution of the Milky Way from the observed chemical abundances. Hence, in the Result Sections we compare the stellar abundance ratios from the MINCE project with the predictions of chemical evolution models. In particular, in this Section we briefly recall the main characteristics of the reference chemical evolution we use in this study for i) the Milky disc and ii) the *Gaia*-Sausage-Enceladus (GSE) accretion event (Belokurov et al. 2018; Haywood et al. 2018; Helmi et al. 2018), respectively.

6.1. Model for the disc components by Spitoni et al. (2021)

Spitoni et al. (2021) presented a revised version of the classical two-infall chemical evolution model (Chiappini et al. 1997) in order to reproduce the Galactic disc components as traced by the APOGEE DR16 (Ahumada et al. 2020) abundance ratios. In this model, the Galactic disc is assumed to be formed by two independent, sequential episodes of gas accretion giving rise to the thick and thin disc components, respectively. As already pointed out by Spitoni et al. (2019b, 2020) and Palla et al. (2020) the signature of a delayed gas-rich merger (i.e. the delay between the two gas infall is $\sim$ 4 Gyr) is imprinted in the APOGEE abundance ratios. We recall that in Spitoni et al. (2021) a Bayesian framework based on MCMC methods has been used to find the best chemical evolution model constrained by APOGEE DR16 [Mg/Fe] and [Fe/H] abundance ratios at different Galactocentric distances. In the solar neighborhood, the dilution effect caused by the second infall produces a characteristic feature in the [α/Fe] and [Fe/H] space. In fact, the late accretion of pristine gas has the effect of decreasing the metallicity of stars born immediately after the infall event, leading to a evolution at nearly constant [α/Fe] since both α and Fe are diluted by the same amount (Spitoni et al. 2019b).

The Scalo (1986) initial stellar mass function (IMF), constant in time and space has been adopted.

The model computed in the solar vicinity (8 kpc) assumes primordial infall for both infall episodes but different star formation efficiencies (SFEs): 2 Gyr^{-1} (thick disc) and 1 Gyr^{-1} (thin disc). We refer the reader to the middle column (model for the solar vicinity) of Table 2 in Spitoni et al. (2021) for the values of the best-fit model parameters as predicted by MCMC calculations: i.e. gas infall timescales, present-day total surface mass density ratio and the delay between the two gas infall. It is worth mentioning that the predicted present-day total surface mass density ratio between thin and thick disc sequences of $5.635^{+0.214}_{-0.162}$ is in very good agreement with the value derived by Fuhrmann et al. (2017) for the local mass density ratio (5.26).

In this paper, we compare observational data for α and iron-peak elements with model predictions in the solar neighbourhood adopting the same nucleosynthesis prescriptions as in Spitoni et al. (2021), i.e. applying the ones suggested by François et al. (2004). This set of yields has been widely used in the past (Cescutti et al. 2007; Mott et al. 2013; Spitoni et al. 2015, 2019a,b) and turned out to be able to reproduce the main chemical abundances of the solar neighbourhood. The elements Na, Al, V, Cr and Cu were not considered in François et al. (2004) and we do not show model results for these elements here.

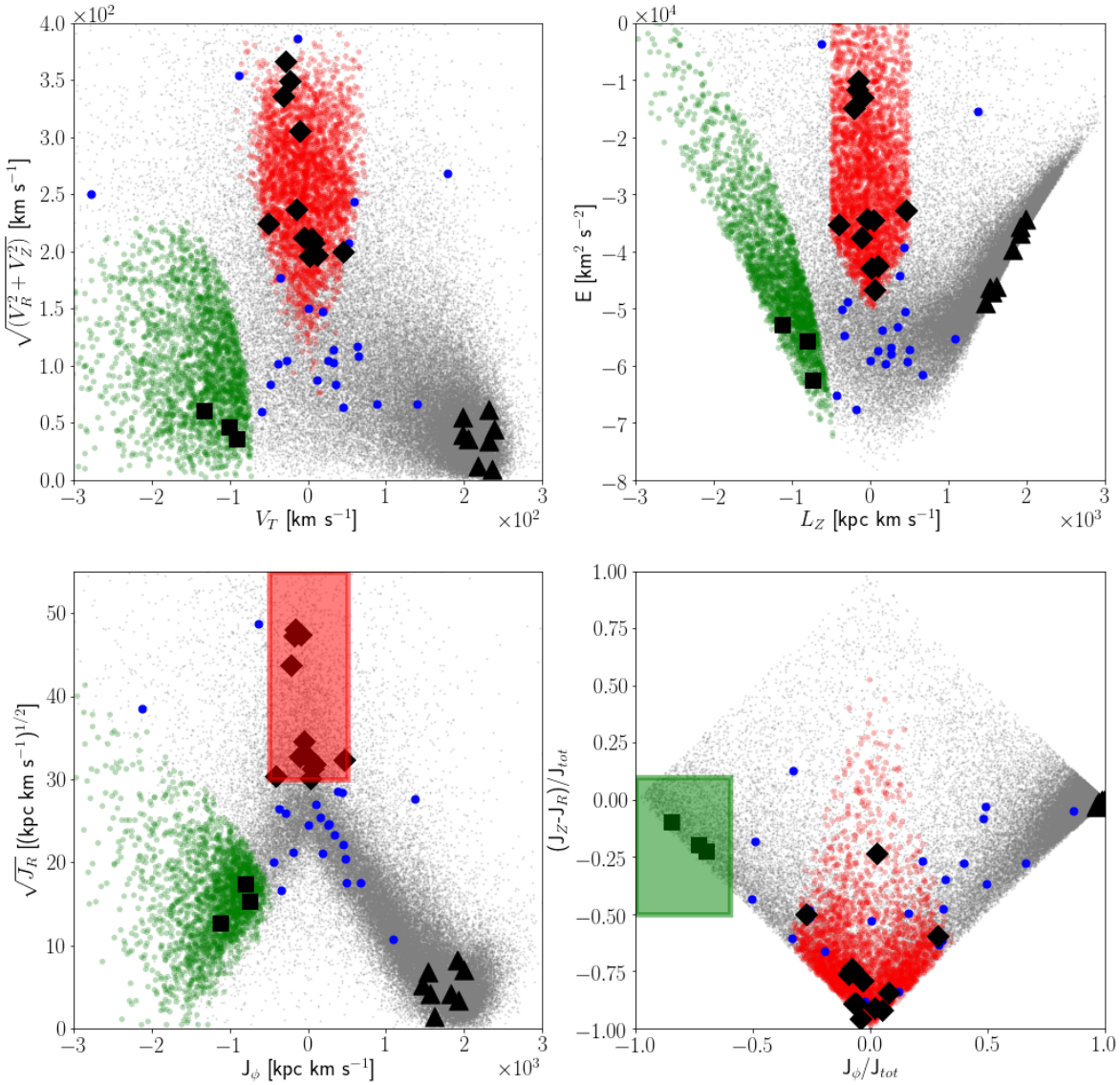

Fig. 4. Target stars kinematic properties are presented in various planes. Program stars are presented as big filled symbols. The background population (gray points) is the "good parallax sample" of Bonifacio et al. (2021b) and is presented for reference. Red filled points in all planes are stars selected from the background population as likely GSE members according to the red shaded box of the bottom-left panel. Green filled points are likely Sequoia members according to the green shaded box in the bottom-right panel. Upper-right: Orbital energy E *vs* angular momentum L$_Z$. Upper-left panel: Toomre diagram ($\sqrt{V_R^2+V_Z^2}$ *vs* V$_T$). Bottom-right panel (action diamond diagram): the difference in the vertical and radial actions (J$_Z$-J$_R$) *vs* the azimuthal action (J$_\phi$=L$_Z$). Quantities are normalized to the total action J$_{tot}$=J$_Z$+J$_R$+|J$_\phi$|. Bottom-left panel: $\sqrt{J_R}$ *vs* L$_Z$. Target stars likely belonging to GSE and Sequoia are marked as black filled diamond and squares, respectively. Targets likely belonging to the thin disc are presented as black filled triangles. Remaining targets are presented as blue filled circles.

6.2. GSE

A large fraction of the halo stars in the solar vicinity are the result of an accretion event, associated to a disrupted satellite, dubbed GSE (Belokurov et al. 2018; Haywood et al. 2018; Helmi et al. 2018). As presented in the previous section, we study the kinematics of our sample and we can determine which are the progenitors of our sample, so if they used to belong to GSE or Sequoia. For this reason we decide to compare our data to a model built to describe the chemical enrichment evolution in GSE. The model and the exact parameters are described in Cescutti et al. (2020), but to summarise the most important feature, its evolu-

Table 2. Cylindrical galactocentric velocity components (V_R, V_T, V_Z), pericentric (r_{peri}) and apocentric (r_{ap}) distances, orbit's eccentricities (ecc.) and maximum height over the galactic plane (Z_{max}) obtained using the Galpy code as described in section 4.3.

Star	V_R km/s	V_T km/s	V_Z km/s	r_{ap} kpc	r_{peri} kpc	ecc.	Z_{max} kpc
BD+034904	-179.50 ± 7.26	52.61 ± 1.76	103.86 ± 3.35	1.15 ± 0.07	13.90 ± 0.46	0.85 ± 0.01	5.61 ± 0.18
BD+0418[b]	190.95 ± 7.09	11.10 ± 9.07	-48.12 ± 3.20	0.20 ± 0.14	13.29 ± 0.53	0.97 ± 0.02	2.58 ± 0.20
BD+062880	-349.70 ± 12.25	-13.19 ± 9.67	-165.05 ± 7.93	0.19 ± 0.12	49.77 ± 10.63	0.99 ± 0.00	21.83 ± 5.15
BD+074625	-29.08 ± 3.55	-278.29 ± 1.54	248.46 ± 0.39	7.57 ± 0.02	40.41 ± 0.86	0.68 ± 0.01	24.78 ± 0.47
BD+112896	122.65 ± 0.52	0.32 ± 3.79	-87.24 ± 1.19	0.01 ± 0.04	8.62 ± 0.04	1.00 ± 0.01	4.32 ± 0.06
BD+132383[c]	1.91 ± 0.45	235.69 ± 0.07	-9.24 ± 0.15	8.19 ± 0.01	9.92 ± 0.02	0.10 ± 0.00	0.88 ± 0.02
BD+203298[b]	335.50 ± 5.25	-22.99 ± 5.07	98.30 ± 7.70	0.30 ± 0.07	30.87 ± 2.28	0.98 ± 0.00	7.04 ± 1.06
BD+214759	-106.37 ± 3.16	33.01 ± 0.11	42.01 ± 1.76	0.63 ± 0.00	9.28 ± 0.08	0.87 ± 0.00	1.53 ± 0.02
BD+242817[c]	54.91 ± 0.92	197.72 ± 0.60	-3.98 ± 1.57	5.73 ± 0.04	8.75 ± 0.01	0.21 ± 0.00	0.61 ± 0.01
BD+254520	150.05 ± 6.23	178.22 ± 4.84	-223.04 ± 9.51	5.60 ± 0.06	23.87 ± 1.84	0.62 ± 0.03	16.57 ± 1.94
BD+312143[a]	-22.14 ± 0.69	-91.74 ± 6.53	28.40 ± 0.71	2.33 ± 0.22	8.90 ± 0.02	0.59 ± 0.03	1.74 ± 0.01
BD+322483	-84.34 ± 2.61	25.28 ± 5.70	61.27 ± 1.42	0.61 ± 0.14	8.36 ± 0.04	0.86 ± 0.03	4.74 ± 0.28
BD+354847	109.43 ± 3.64	19.10 ± 3.14	-98.70 ± 4.69	0.38 ± 0.06	9.82 ± 0.17	0.92 ± 0.01	4.37 ± 0.44
BD+393309[b]	207.09 ± 1.80	7.16 ± 0.90	-11.00 ± 1.30	0.11 ± 0.01	12.16 ± 0.10	0.98 ± 0.00	1.16 ± 0.01
BD+412520	45.10 ± 0.65	63.42 ± 2.27	108.43 ± 1.17	1.68 ± 0.05	8.44 ± 0.02	0.67 ± 0.01	4.61 ± 0.11
BD+482167	-102.66 ± 2.48	32.19 ± 3.42	-11.10 ± 1.89	0.65 ± 0.07	9.42 ± 0.06	0.87 ± 0.01	2.18 ± 0.09
BD-003963[c]	31.86 ± 0.17	205.68 ± 0.05	17.30 ± 0.06	6.25 ± 0.01	8.08 ± 0.00	0.13 ± 0.00	0.32 ± 0.00
BD-004538	164.76 ± 3.70	-35.84 ± 4.11	65.71 ± 2.39	0.74 ± 0.09	11.05 ± 0.17	0.87 ± 0.01	4.48 ± 0.06
BD-073523	98.45 ± 5.64	65.21 ± 4.10	46.18 ± 1.06	1.32 ± 0.10	8.64 ± 0.10	0.74 ± 0.02	2.22 ± 0.05
HD165400[c]	-11.43 ± 0.11	217.20 ± 0.31	-4.44 ± 0.28	7.01 ± 0.03	7.64 ± 0.02	0.04 ± 0.00	0.21 ± 0.00
HD115575[a]	-41.75 ± 2.61	-100.62 ± 7.76	20.72 ± 4.20	2.20 ± 0.21	7.61 ± 0.03	0.55 ± 0.03	1.35 ± 0.03
HD130971[c]	-39.22 ± 0.22	197.81 ± 0.63	8.35 ± 0.30	5.71 ± 0.04	7.97 ± 0.02	0.16 ± 0.00	0.65 ± 0.01
HD138934[c]	-29.60 ± 0.27	232.14 ± 0.23	17.50 ± 0.13	7.49 ± 0.01	9.50 ± 0.01	0.12 ± 0.00	0.41 ± 0.00
HD139423	-345.55 ± 6.84	-88.84 ± 10.14	76.66 ± 2.39	1.50 ± 0.15	36.97 ± 3.53	0.92 ± 0.00	17.66 ± 1.43
HD142614[b]	331.80 ± 2.36	-31.19 ± 4.77	-51.67 ± 4.14	0.47 ± 0.07	26.85 ± 0.47	0.97 ± 0.00	11.05 ± 0.12
HD143348	54.52 ± 0.90	87.65 ± 3.21	38.02 ± 2.57	1.86 ± 0.08	8.02 ± 0.00	0.62 ± 0.01	1.19 ± 0.08
HD208316	-58.60 ± 4.63	-58.91 ± 6.55	-12.86 ± 4.13	1.14 ± 0.15	7.77 ± 0.04	0.74 ± 0.03	1.10 ± 0.10
HD238439[b]	191.91 ± 6.52	-50.25 ± 12.20	116.43 ± 6.96	1.10 ± 0.29	15.41 ± 1.16	0.87 ± 0.02	6.86 ± 0.76
HD87740[c]	-62.00 ± 0.56	232.26 ± 0.21	-2.20 ± 0.12	7.20 ± 0.01	11.36 ± 0.02	0.22 ± 0.00	0.61 ± 0.01
HD91276[c]	44.29 ± 0.63	238.94 ± 0.13	2.56 ± 0.37	7.79 ± 0.00	11.43 ± 0.05	0.19 ± 0.00	0.81 ± 0.01
HD354750	240.06 ± 6.94	58.46 ± 6.18	41.90 ± 0.41	0.87 ± 0.10	12.61 ± 0.41	0.87 ± 0.02	2.51 ± 0.21
TYC2588-1386-1	4.08 ± 12.41	-48.65 ± 3.54	-83.86 ± 6.18	1.96 ± 0.03	8.80 ± 0.39	0.64 ± 0.02	6.90 ± 0.07
TYC3085-119-1	-22.21 ± 0.51	139.98 ± 0.09	-62.56 ± 0.12	3.71 ± 0.00	7.91 ± 0.00	0.36 ± 0.00	1.68 ± 0.01
TYC1008-1200-1[b]	365.43 ± 3.42	-28.81 ± 4.85	-27.82 ± 3.16	0.33 ± 0.05	29.71 ± 0.60	0.98 ± 0.00	5.52 ± 0.19
TYC2113-471-1	74.56 ± 2.29	-27.53 ± 1.28	-73.78 ± 1.30	0.48 ± 0.03	7.29 ± 0.05	0.88 ± 0.01	2.22 ± 0.06
TYC2228-838-1[b]	195.91 ± 10.10	2.14 ± 9.27	-3.21 ± 4.35	0.04 ± 0.10	13.19 ± 0.79	0.99 ± 0.01	2.37 ± 0.21
TYC2824-1963-1[b]	185.87 ± 5.74	45.06 ± 11.94	-73.40 ± 3.13	1.08 ± 0.29	16.57 ± 0.65	0.88 ± 0.04	4.87 ± 0.60
TYC3944-698-1	-83.95 ± 2.19	11.73 ± 1.87	-23.89 ± 1.16	0.22 ± 0.04	9.54 ± 0.10	0.95 ± 0.01	1.06 ± 0.01
TYC4001-1161-1[b]	-305.15 ± 3.81	-10.34 ± 4.63	11.49 ± 1.67	0.17 ± 0.07	28.67 ± 1.09	0.99 ± 0.01	0.88 ± 0.04
TYC4221-640-1[b]	-195.33 ± 8.35	4.23 ± 4.92	81.33 ± 9.43	0.14 ± 0.54	15.33 ± 1.15	0.98 ± 0.05	13.93 ± 2.40
TYC4267-2023-1[a]	-25.68 ± 1.12	-132.41 ± 0.77	54.88 ± 1.39	3.56 ± 0.05	8.65 ± 0.01	0.42 ± 0.01	1.41 ± 0.05
TYC4331-136-1	-4.74 ± 2.54	35.36 ± 4.54	83.62 ± 3.38	0.89 ± 0.11	9.81 ± 0.08	0.83 ± 0.02	4.53 ± 0.42
TYC4584-784-1	-100.72 ± 2.88	-38.07 ± 3.71	-15.45 ± 4.24	0.86 ± 0.09	11.01 ± 0.14	0.85 ± 0.01	1.77 ± 0.08
TYC565-1564-1[b]	236.11 ± 10.06	-14.20 ± 12.56	-17.13 ± 8.83	0.24 ± 0.20	14.78 ± 1.21	0.97 ± 0.02	5.27 ± 0.58
TYC33-446-1	-16.17 ± 1.51	45.68 ± 8.91	61.42 ± 1.57	1.42 ± 0.28	10.35 ± 0.13	0.76 ± 0.04	4.93 ± 0.20
TYC4-369-1[b]	194.02 ± 9.62	-5.07 ± 18.12	-86.58 ± 5.91	0.10 ± 0.26	16.10 ± 1.37	0.99 ± 0.03	5.88 ± 0.75

(a) Sequoia candidate.
(b) GSE candidate.
(c) Thin disc.

tion is similar to a dwarf spheroidal galaxy (Lanfranchi et al. 2008), so less massive than our Galaxy by around a factor of 30 at the beginning. However, given its galactic winds and the less efficient star formation ending 6 Gyr ago, its stellar content is only a hundredth of the Galactic stellar mass. The nucleosynthesis adopted is basically the same of François et al. (2004), to be consistent with the model in Spitoni et al. (2021). The only difference is that the iron production assumed for SNe II is 0.07 $M_\odot$ for the SNe II (Limongi & Chieffi 2018, see) in Cescutti et al. (2020), which is about a factor of 2 lower than the iron consider in François et al. (2004). For this reason, we decide to decrease accordingly the yields for iron peak elements from massive stars by a factor of 2; any other deviation is described for the specific element.

Table 3. Stellar orbital energies (E), vertical component of the angular momentum (L_Z) and radial and vertical actions (J_R, J_Z).

Star	E km^2 s^{-2}	L_Z kpc km/s	J_R kpc km/s	J_Z kpc km/s
BD+034904	-39338.09 ± 1127.74	434.30 ± 13.76	809.03 ± 52.92	145.72 ± 15.00
BD+0418[b]	-42513.31 ± 1635.62	92.87 ± 75.73	1016.43 ± 71.04	45.15 ± 2.83
BD+062880	5622.52 ± 5730.94	-92.51 ± 67.22	3584.74 ± 667.63	184.49 ± 8.93
BD+074625	1544.83 ± 599.14	-2125.03 ± 10.56	1481.70 ± 53.38	698.28 ± 2.18
BD+112896	-59067.51 ± 243.19	2.27 ± 27.22	599.82 ± 8.54	182.99 ± 3.29
BD+132383[c]	-36851.45 ± 67.52	1924.87 ± 1.44	11.86 ± 0.22	14.82 ± 0.64
BD+203298[b]	-10201.18 ± 2540.13	-156.84 ± 33.80	2311.39 ± 141.13	62.76 ± 7.73
BD+214759	-57871.41 ± 351.37	265.05 ± 0.98	608.16 ± 7.09	33.60 ± 1.12
BD+242817[c]	-46355.49 ± 67.06	1532.55 ± 4.89	47.22 ± 1.59	9.15 ± 0.24
BD+254520	-15380.65 ± 2293.01	1376.01 ± 37.05	759.95 ± 112.46	672.75 ± 63.24
BD+312143[a]	-55728.06 ± 721.22	-802.73 ± 58.57	301.37 ± 25.08	45.69 ± 0.46
BD+322483	-59630.68 ± 255.87	189.39 ± 43.00	443.13 ± 15.36	216.69 ± 17.41
BD+354847	-53688.33 ± 889.31	157.10 ± 25.69	644.01 ± 15.53	165.57 ± 22.46
BD+393309[b]	-46738.94 ± 340.89	54.40 ± 6.83	977.79 ± 11.03	15.09 ± 0.28
BD+412520	-57201.08 ± 24.02	499.68 ± 17.95	309.05 ± 5.88	226.49 ± 7.52
BD+482167	-56753.65 ± 246.36	261.40 ± 27.62	598.58 ± 16.69	56.42 ± 2.97
BD-003963[c]	-47007.38 ± 19.34	1565.26 ± 0.80	17.55 ± 0.11	3.27 ± 0.02
BD-004538	-48836.38 ± 650.68	-286.84 ± 32.93	670.27 ± 1.88	141.76 ± 5.30
BD-073523	-59178.43 ± 310.18	477.42 ± 31.41	419.23 ± 22.81	65.91 ± 1.22
HD165400[c]	-46100.83 ± 135.27	1620.05 ± 4.77	2.04 ± 0.08	1.64 ± 0.07
HD115575[a]	-62436.30 ± 569.91	-740.81 ± 55.13	235.95 ± 25.27	37.22 ± 1.08
HD130971[c]	-48991.09 ± 173.44	1469.11 ± 7.06	28.05 ± 0.68	11.49 ± 0.35
HD138934[c]	-39560.78 ± 62.24	1828.31 ± 2.59	17.45 ± 0.11	4.24 ± 0.08
HD139423	-3655.31 ± 3049.07	-632.91 ± 69.96	2369.28 ± 212.44	232.20 ± 6.38
HD142614[b]	-14886.95 ± 619.65	-213.86 ± 31.79	1910.64 ± 22.81	162.79 ± 7.20
HD143348	-61607.48 ± 150.19	669.01 ± 25.39	308.18 ± 9.87	28.49 ± 2.82
HD208316	-65109.88 ± 682.23	-437.14 ± 47.53	399.44 ± 23.29	25.56 ± 3.68
HD238439[b]	-35278.11 ± 3032.28	-409.69 ± 100.28	920.41 ± 28.28	171.13 ± 14.78
HD87740[c]	-35668.33 ± 20.63	1917.26 ± 0.98	67.49 ± 0.92	6.29 ± 0.15
HD91276[c]	-34291.52 ± 94.96	1994.38 ± 2.18	49.31 ± 1.25	10.46 ± 0.24
HD354750	-44243.32 ± 1272.11	379.15 ± 41.22	813.65 ± 51.11	48.93 ± 4.02
TYC2588-1386-1	-54671.06 ± 1380.35	-339.89 ± 29.48	277.00 ± 34.50	410.02 ± 38.02
TYC3085-119-1	-55313.29 ± 10.17	1085.79 ± 1.01	114.68 ± 0.30	53.54 ± 0.38
TYC1008-1200-1[b]	-11569.16 ± 711.06	-173.10 ± 26.17	2235.15 ± 29.20	46.91 ± 0.92
TYC2113-471-1	-67655.11 ± 154.57	-187.60 ± 8.12	452.52 ± 10.74	82.13 ± 3.89
TYC2228-838-1[b]	-42910.75 ± 2446.65	18.04 ± 78.59	1053.15 ± 62.93	40.17 ± 1.85
TYC2824-1963-1[b]	-32798.81 ± 1356.66	464.84 ± 118.00	1047.38 ± 105.01	92.10 ± 11.10
TYC3944-698-1	-57398.19 ± 497.16	102.71 ± 17.00	728.08 ± 0.83	18.32 ± 0.15
TYC4001-1161-1[b]	-12998.56 ± 1348.15	-95.09 ± 42.13	2248.08 ± 101.24	2.58 ± 0.06
TYC4221-640-1[b]	-34552.60 ± 3168.92	39.58 ± 47.04	905.59 ± 31.04	557.89 ± 175.20
TYC4267-2023-1[a]	-52771.29 ± 211.40	-1128.09 ± 8.00	161.60 ± 3.79	36.50 ± 2.29
TYC4331-136-1	-53172.43 ± 407.65	341.14 ± 41.80	546.21 ± 17.06	175.52 ± 23.48
TYC4584-784-1	-50164.69 ± 653.59	-366.30 ± 36.51	696.68 ± 10.85	33.24 ± 1.78
TYC565-1564-1[b]	-37633.12 ± 3170.28	-104.55 ± 92.33	1071.44 ± 47.87	115.58 ± 6.37
TYC33-446-1	-50421.65 ± 152.82	446.14 ± 82.86	490.18 ± 46.82	179.34 ± 5.00
TYC4-369-1[b]	-34227.63 ± 3291.84	-44.03 ± 158.21	1197.95 ± 78.51	119.72 ± 9.06

(a) Sequoia candidate.
(b) GSE candidate.
(c) Thin disc.

7. Results for α-elements

In Figs. 5, 6, 7, 8, 10 and 11, we show our results for the α-elements O, Mg, Si, Ca and Ti, respectively. In these plot, we include only stars selected with mince2 selection (and two stars chosen thanks to the APOGEE survey) and this has provided stars belonging either to the halo or to the substructures GSE and Sequoia that we distinguish thanks to the color-coding.

Searching for specific differences between halo stars and Sequoia or GSE, but also between GSE and Sequoia, we cannot find within α-element abundances any clear signal, all the stars seem to share the same plateau with some dispersion. Surely, the star with the lowest [α/Fe] and a relative low [Fe/H] (~ -2.25) belongs to GSE. The other feature that we can be acknowledged is that at [Fe/H]~ -1.5, GSE stars show on average a lower [α/Fe].

Table 4. Sulphur abundances obtained from lines of Multiplet 1 in spectra obtained at CFHT by ESPaDOnS

ID	A(S)$_{LTE}$	$A(S)_{NLTE}$	[S/Fe]$_{NLTE}$
BD+39−3309	5.33	5.00	0.42
BD+31−2143	5.50	5.20	0.41
BD+32−2483	5.76	5.51	0.60
BD+20−3298	5.89	5.82	0.61
BD+48−2167	5.87	5.57	0.69
TYC 3085−119−1	6.05	5.79	0.14

Table 5. Solar abundances.

Element	A(X)	Reference
C	8.50	Caffau et al. (2011)
O	8.76	Caffau et al. (2011)
Na	6.30	Lodders et al. (2009)
Mg	7.54	Lodders et al. (2009)
Al	6.47	Lodders et al. (2009)
Si	7.52	Lodders et al. (2009)
S	7.16	Caffau et al. (2011)
Ca	6.33	Lodders et al. (2009)
Sc	3.10	Lodders et al. (2009)
Ti	4.90	Lodders et al. (2009)
V	4.00	Lodders et al. (2009)
Cr	5.64	Lodders et al. (2009)
Mn	5.37	Lodders et al. (2009)
Fe	7.52	Caffau et al. (2011)
Co	4.92	Lodders et al. (2009)
Ni	6.23	Lodders et al. (2009)
Cu	4.21	Lodders et al. (2009)
Zn	4.62	Lodders et al. (2009)

Overall, this outcome is confirmed by the models results. In the models, the chemical differences expected between GSE and the disc of our Galaxy reside in the [α/Fe] vs [Fe/H] observed at [Fe/H]> −1.5, where the two models do show a clear difference. However, most of our stars have lower metallicity so they are not expected to be firmly distinguished chemically. Between the two models describing the chemical evolution of the discs of our Galaxy and the GSE, there is also an offset for what concern the plateau, with the one for GSE on average slightly (0.1-0.2) above the trend of the discs model. This outcome is most likely connected to the choice of the iron yields. Probably, more interesting is that the models predict a slightly different steepness in the trend of α in the range −2.5<[Fe/H]< −1.5, with GSE having a more negative behaviour. A hint for this can be found in the fact that GSE stars show on average a lower [α/Fe] mentioned before. Surely more data may help confirming this feature.

In Fig. 9, we decided to present our results for [Ca/Fe] compared to the results obtained by Ishigaki et al. (2012) for this element The abundances taken from by Ishigaki et al. (2012) were re-normalised to our solar abundances to avoid spurious offsets. Overall our results are in excellent agreement with the abundances obtained for halo stars by Ishigaki et al. (2012), although they can comprised also stars of GSE and Sequoia. The main visible difference is that this sample extends further at metallicity up to [Fe/H]∼ −1 (with two stars almost at [Fe/H]∼ −0.5).

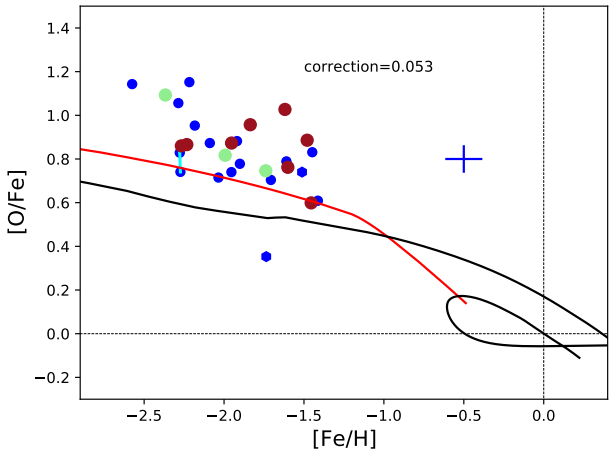

Fig. 5. [O/Fe] vs [Fe/H] abundances measured in the MINCE stars: blue solid dots stars selected with the mince2 selection, hexagons from APOGEE. Cyan lines connect the abundances measured for the same stars with spectra taken from two facilities. The colors of the dot refer to the substructures to which they belong: red for GSE, light green for Sequoia and blue for the remaining stars. The black lines refers to the chemical evolution model by Spitoni et al. (2021) for the discs of our Galaxy, whereas the red line is a model for GSE (Cescutti et al. 2020).

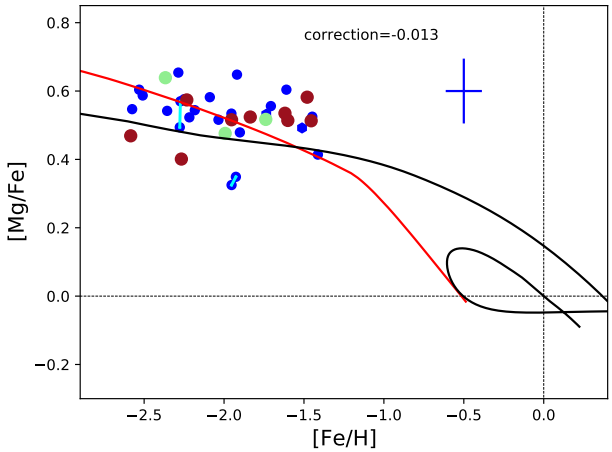

Fig. 6. The same as Fig.5, but for [Mg/Fe] vs [Fe/H].

8. Results for sodium at aluminum

In Fig.12, we present the plot for sodium. It presents a dispersion in the data that can be at least partially due to NLTE effects; surely, it is an element where NLTE effects play an important role (see Sect. 10 and Table 6). An important feature is visible in the comparison between halo stars and GSE and Sequoia stars. In our sample, we have three stars enhanced in sodium and they all belong to the halo. Given the limited sample, not strong conclusions can be obtained, but we will follow up this signature within our future MINCE stars. We show in Fig. 13 the ratio obtained for aluminum; the dispersion is not present for this element but again four stars show an enhancement of [Al/Fe]>0.4 and again none of these stars belong to GSE or Sequoia.

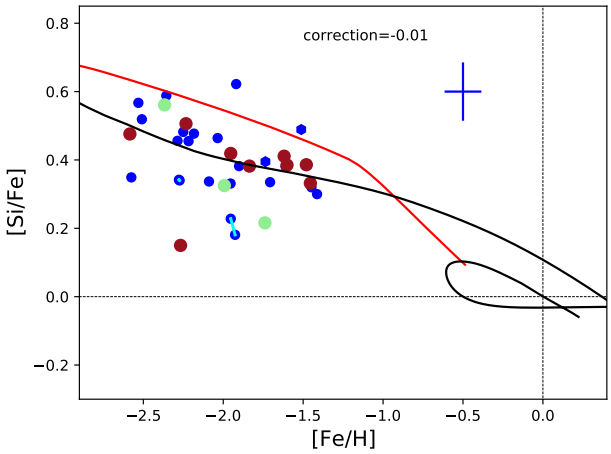

Fig. 7. The same as Fig.6, but for [Si/Fe] vs [Fe/H].

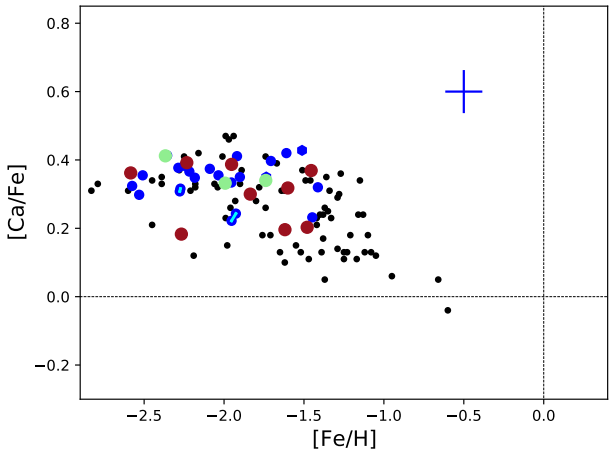

Fig. 9. Similar to the Fig.8, but without the line of models and with the results by Ishigaki et al. (2012) for halo star with black symbols.

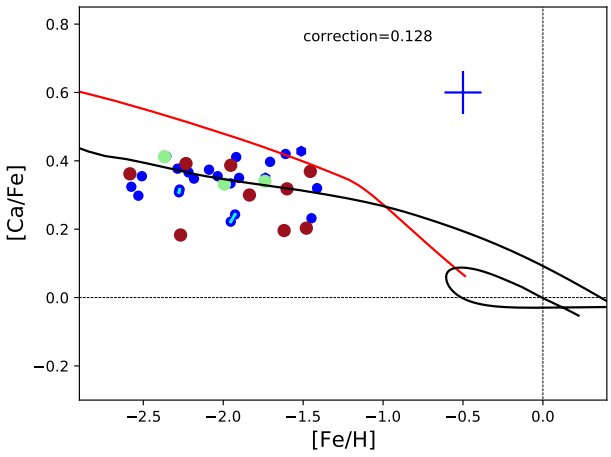

Fig. 8. The same as Fig.6, but for [Ca/Fe] vs [Fe/H].

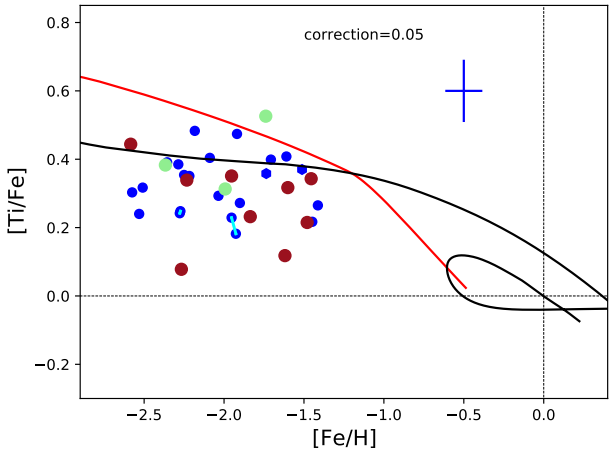

Fig. 10. The same as Fig.6, but for [Ti/Fe] vs [Fe/H].

9. Results for iron-peak elements

In Figs. 14-22, we present the results that we have obtained for the iron peak elements. Among the iron peak elements, copper presents the largest offset among the chemical abundance measurements of the two duplicate stars. The difference is anyway <0.2 dex and for most of the other elements is well below 0.1 dex.

Not surprisingly, most of the iron peak elements have a chemical evolution similar to the one of iron, being produced in a similar manner by SNe II and SNe Ia and therefore presenting a solar ratio. The most intriguing exceptions are manganese and copper that in the stellar atmosphere of our sample have negative abundance ratios compared to iron (normalised to the Sun). Manganese is a remarkable element, because it has a single stable isotope and for this reason its production is quite sensitive to the explosion conditions. In fact, theoretical computations have found that different classes of supernovae Ia are expected to produce different amount of manganese. Thanks to this characteristic, it was possible to exclude the exclusive enrichment of single degenerate SNe Ia from chemical evolution modelling. It was also possible to evaluate the fraction of different SNe Ia contributing to the enrichment of manganese Seitenzahl et al. (2013); **?**, although the impact of NLTE in the determination and also the exact metallicity dependence of the yields of SNe II can impact the exact determination of this fraction. Moreover, the differential enrichment of manganese by the SNe Ia classes may also produce a spread in the enrichment, as shown in Cescutti & Kobayashi (2017).

On the other hand, copper is not expected to be significantly produced by SNe Ia, and the rise toward the solar metallicity is driven by a strong metal dependency in SNe II Timmes et al. (1995). Contrary to copper and manganese, scandium presents a behaviour similar to the one of the α-elements, with a [Sc/Fe]>0 for [Fe/H]< -1. This is controversial, in the sense that the results from François et al. (2004) seem to indicate a behaviour similar to standard iron peak elements, so an about constant [Sc/Fe]$\sim$ 0. In this case, it is difficult also to rely to theoretical nucleosynthesis expectations, since the yields for scandium are usually too low by 1 dex (Romano et al. 2010; Kobayashi et al. 2011).

The chemical evolution deduced from the MINCE stars for the rest of our iron peak elements appears to be remarkably similar to iron. We also note that our estimates for Cr I and Cr II are in agreement, contrary to the discrepancy observed in the Ishigaki et al. (2013) data for this element between ionized and neu-

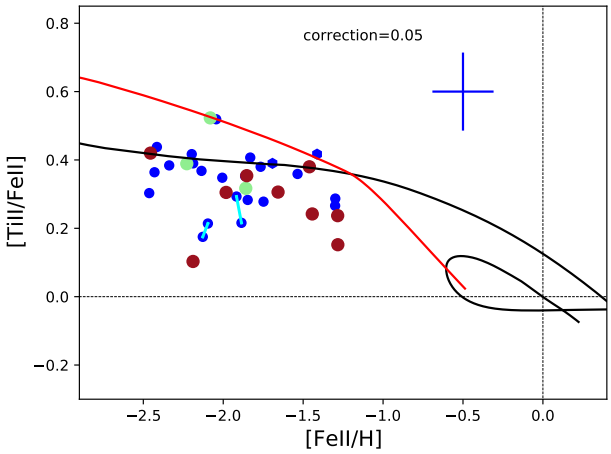

Fig. 11. The same as Fig.6, but for [Ti II/Fe II] vs [Fe II/H].

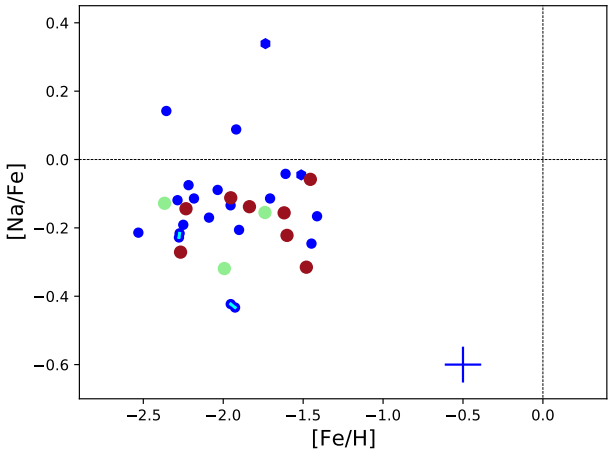

Fig. 12. The same as Fig.5, but for [Na/Fe] vs [Fe/H].

tral species; in fact, for this comparison data set it is present an average [Cr I/Fe I] ratio slightly below solar ratio, and slightly above for [Cr II/Fe II]. Also the different selection of Cr lines shall be accounted for the discrepancy as also remarked in **?**. This trend of [Cr/Fe] is also compatible to the results obtained applying NLTE corrections for chromium in Bergemann & Cescutti (2010).

Four stars appear to be enhanced in vanadium for [Fe/H]< −1.5 compared to rest of the sample. Moreover, the stars with high [V/Fe] at [Fe/H]∼ −2.5 shows also a high [Ni/Fe] and [Zn/Fe](and a low [Sc II/Fe II]). Notably, this star belong the GSE substructure.

We show the chemical evolution tracks also for iron peak elements, but we are afraid that the yields assumed (we recall that we use François et al. 2004) are not the final answer, as shown already for manganese (Cescutti et al. 2008; Seitenzahl et al. 2013; Cescutti & Kobayashi 2017) and possibly true for other elements. Clearly, the chemical evolution models can *only* be as good as their nucleosynthesis input and the iron peak nucleosynthesis is not so well understood at present (see for example Fig. 15 of Kobayashi et al. 2011). Still, the chemical evolution results for GSE seem to reproduce the observed ratios at least for manganese, cobalt and nickel, indicating that the role and timescale of SNe Ia are well considered.

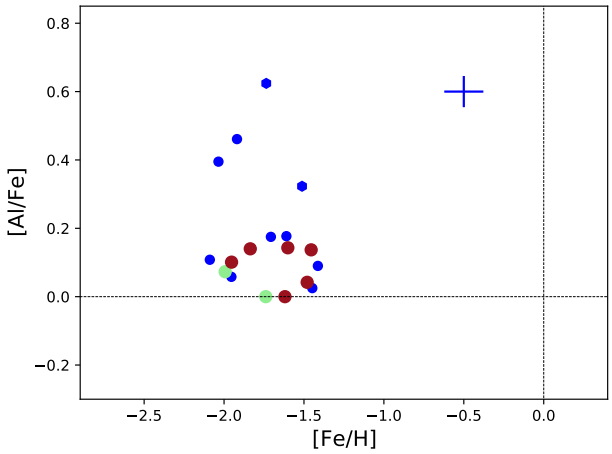

Fig. 13. The same as Fig.6, but for [Al/Fe] vs [Fe/H].

Again we do not see in the data any significant trend or offset between halo stars and GSE stars. Regarding Sequoia's stars, the abundance ratios of V, Cr, Mn and Co compared to Fe are increasing toward higher metallicity, whereas the opposite happens to Zn and Ni. Clearly with 3 stars, these trends cannot considered significant, but we will keep trace of this hint within future MINCE papers.

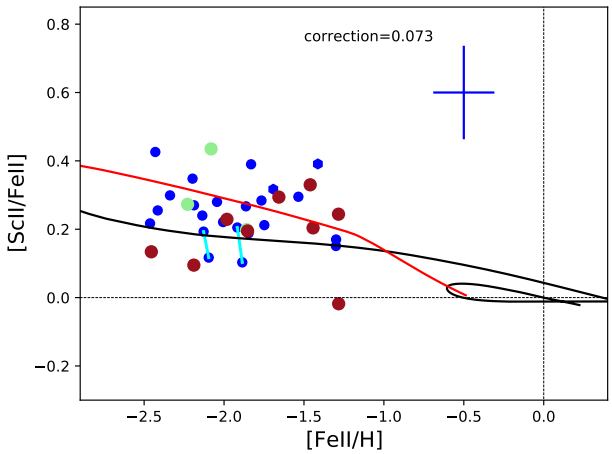

Fig. 14. The same as Fig. 6, but for [Sc II/Fe II] vs [FeII /H].

10. NLTE corrections

Depending on the exact choice of lines combined with the stellar parameters and the abundances itself, some elemental abundances suffer from the 1D, LTE assumptions, while others remain good chemical tracers. Several studies target such improvements computing either NLTE or 3D abundances (or both – see e.g. Amarsi et al. 2019; Bergemann et al. 2017, 2019; Caffau et al. 2008; Lind et al. 2012; Mashonkina 2020; Sitnova et al. 2016; Steffen et al. 2015).

The recent study by Hansen et al. (2020) presented corrected abundances for most of elements presented here, with the ex-

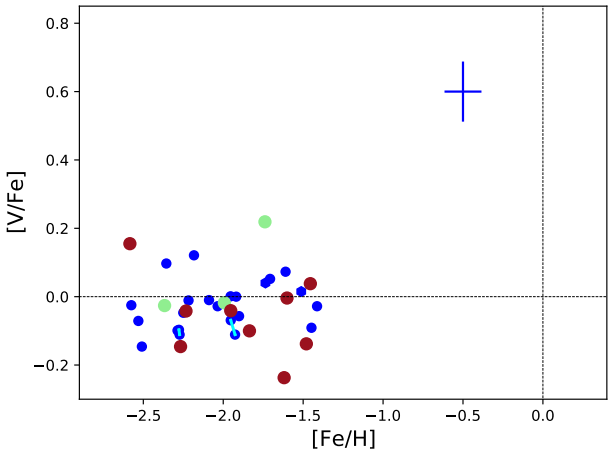

Fig. 15. Similar as Fig.7, but for [V/Fe] vs [Fe/H].

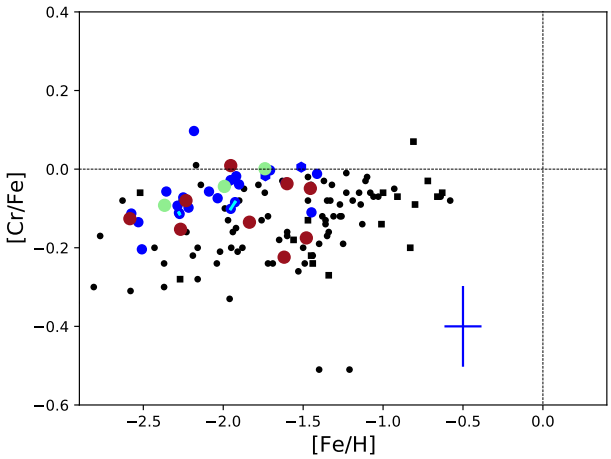

Fig. 16. Same as Fig.15, but for [Cr/Fe] vs [Fe/H]. In this figure we also show a comparison sample from Ishigaki et al. (2013).

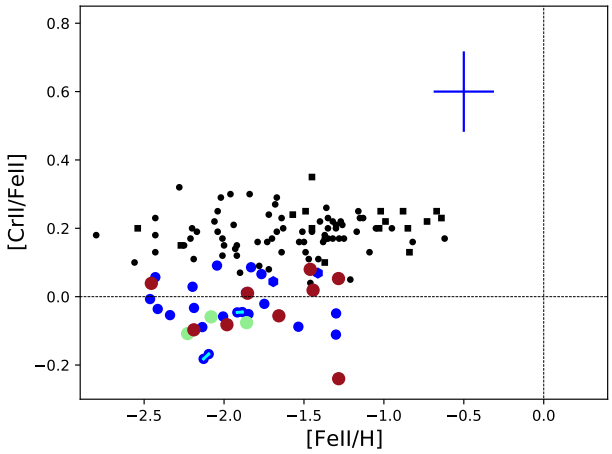

Fig. 17. Same as Fig.16, but for [Cr II/Fe] vs [Fe II/H].

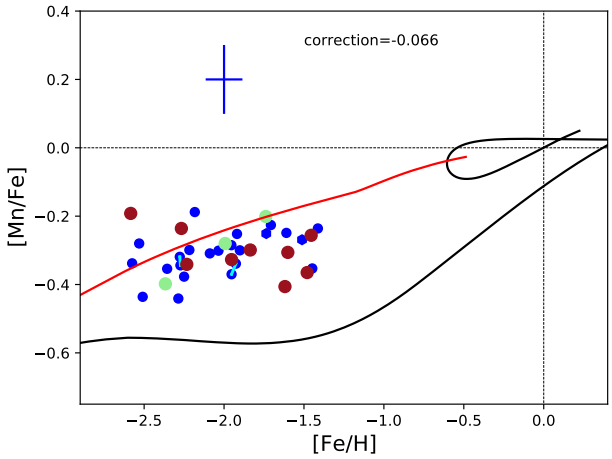

Fig. 18. Similar as Fig.6, but for [Mn/Fe] vs [Fe/H].

ception of Al. Owing to the overlap in stellar parameter space, we use their NLTE computations as an indication of where corrections for the LTE assumptions would affect the LTE abundances most. A full abundance correction will be presented in a forth coming paper. A few stars show a good agreement (overlap) in stellar parameters and the corrections, which are sensitive to the stellar parameters, can therefore help us assess the level or at least direction the NLTE corrections would bring the corrected NLTE abundances in. From Hansen et al. (2020) - BD-10_3742 (T/logg/[Fe/H]/Vt: 4678 ± 120/1.38 ± 0.04/ − 1.96 ± 0.07/1.9 ± 0.1) and BD-12_106 (4889 ± 50/2.03 ± 0.05/ − 2.11 ± 0.04/1.5 ± 0.2) come close to two of the MINCE programme stars, namely BD+07_4625 (4757/1.64/ − 1.93/1.86) and BD+39_3309 (4909/1.73/ − 2.58/1.94). To estimate the order of magnitude of the corrections, we read off the NLTE corrections from their Table A.1, and we note that these are only approximate as the corrections also strongly depend on the use of lines and the actual size of the abundances as well. The NLTE corrections are presented as ΔNLTE = NLTE − LTE.

From Table 6, it is clearly seen that the largest corrections for such stars are obtained for Na, (SiI, K, TiI), Cr, Mn, and Co (especially the latter). In the case of Na, over recombination

Table 6. Approximate NLTE corrections for two MINCE stars based on Hansen et al. (2020, H2020).

H2020	BD-10_3742	BD-12_106
MINCE	BD+07_4625	BD+39_3309
Element	$\Delta NLTE$	$\Delta NLTE$
CI	−0.06	−0.04
OI	−0.10	−0.10
NaI	−0.30	−0.21
MgI	0.03	0.08
SiI	−0.13	−0.12
SI	—	0.00
KI	−0.16	−0.14
CaI	0.09	0.04
ScII	—	−0.03
TiI	0.14	0.14
TiII	−0.03	−0.04
CrI	0.16	0.21
MnI	0.00	0.18
FeI	0.08	0.11
FeII	0.00	0.02
CoI	0.55	0.73

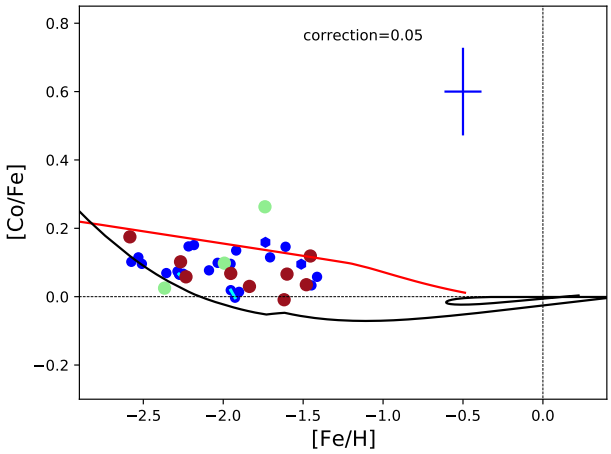

Fig. 19. Same as Fig.18, but for [Co/Fe] vs [Fe/H].

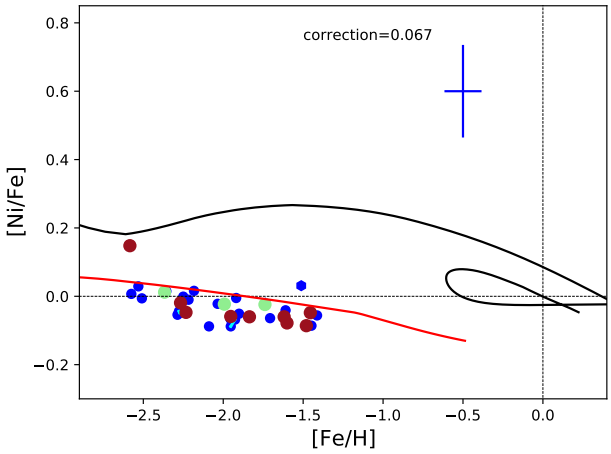

Fig. 20. Same as Fig.18, but for [Ni/Fe] vs [Fe/H].

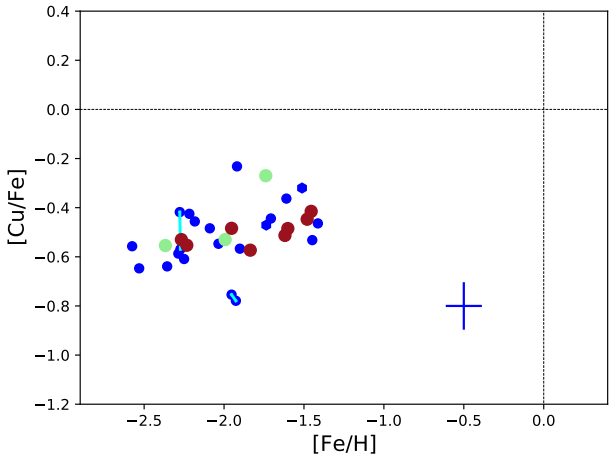

Fig. 21. Same as Fig.15, but for [Cu/Fe] vs [Fe/H].

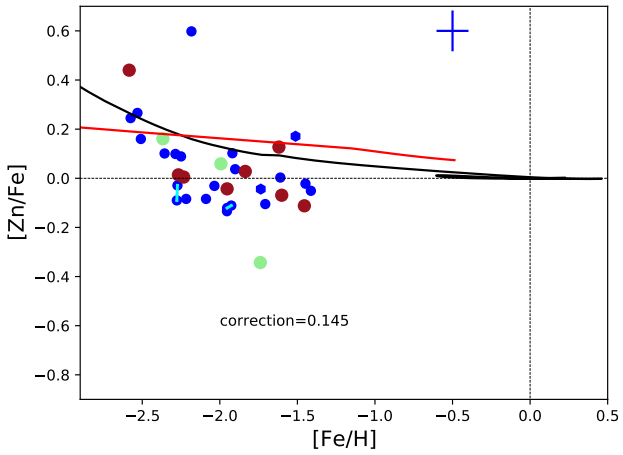

Fig. 22. Same as Fig.18, but for [Zn/Fe] vs [Fe/H].

leads to strengthening of the lines and negative NLTE corrections. For K the corrections also exceed ±0.1dex, and here they are dictated by the source function, and caused by resonance line scattering, where similar to Na D lines an over population of the ground states shift the line formation outwards. This in turn deepens the K lines, so the effect is governed by the radiation field and rates. In this case, the values were interpolated using the grid from Reggiani et al. (2019). The corrections are positive for Si, where NLTE computations lead to weakened Ti I lines and hence result in positive corrections. Here the corrections are photoionisation dominated, which means that they are sensitive to overionisation driven by a non-local high-energy radiation field. This leads to weakening of low-excitation potential lines and in turn positive NLTE corrections (as LTE underestimates their abundances). However, the largest corrections are seen for the Fe-peak elements (especially Co). Detailed NLTE studies for Mn and Co are important to properly understand their chemical evolution (e.g. Eitner et al. 2020).

11. Conclusions

We describe the method adopted in the MINCE project to select our sample, determine the stellar atmosphere of our stellar

targets and measure at at intermediate-low metallicity the chemical abundances of several α-elements and iron peak elements, Na and Al. The first selection criteria, based solely on Starhorse Anders et al. (2019) was not ideal. It allowed to select properly the characteristics of the stars in term of log g and $T_{\rm eff}$. It also correctly determines metal-poor stars, but not as metal-poor as requested by our project ([Fe/H]< -1). For this reason, we implement also a selection based on kinematics by requiring the $v_{\rm tot} > 200$ km/s, so stars not belonging to discs of our Galaxy. With this new constraint, the selection is successful in finding stars with metallicities below [Fe/H]< -1 and therefore within the MINCE metallicity range. Thanks to Gaia data, we are also able to distinguish among our sample, stars belonging to GSE (12) and Sequoia (3). We did not have find specific trends and offsets compared to the sample of halo stars (defined as those not belonging neither to GSE nor Sequoia). This is not completely unexpected given that the sample is still small; moreover also the chemical evolution results did not predict important feature in the metallicity range that we explore, but for slightly more metal rich objects.

The comparison with a similar sample produced by Ishigaki et al. (2012) and Ishigaki et al. (2013) has shown that our approach is sound and our results are valid. The determination of abundances from two stars from spectra taken by different spectrographs produce the same results, showing that our outcome are solid and independent of the facility used. Thanks to this outcome, we can move forward, extending our chemical abundance measurements to neutron capture elements that are the main focus of the MINCE project.

Acknowledgements. We gratefully acknowledge support from the French National Research Agency (ANR) funded project "Pristine" (ANR-18-CE31-0017). This work has made use of data from the European Space Agency (ESA) mission *Gaia* (https://www.cosmos.esa.int/gaia), processed by the *Gaia* Data Processing and Analysis Consortium (DPAC, https://www.cosmos.esa.int/web/gaia/dpac/consortium). Funding for the DPAC has been provided by national institutions, in particular the institutions participating in the *Gaia* Multilateral Agreement. This research has made use of the SIMBAD database, operated at CDS, Strasbourg, France.

References

Ahumada, R., Allende Prieto, C., Almeida, A., et al. 2020, ApJS, 249, 3
Amarsi, A. M., Nissen, P. E., & Skúladóttir, Á. 2019, A&A, 630, A104
Anders, F., Khalatyan, A., Chiappini, C., et al. 2019, A&A, 628, A94
Barbá, R. H., Minniti, D., Geisler, D., et al. 2019, ApJ, 870, L24
Belokurov, V., Erkal, D., Evans, N. W., Koposov, S. E., & Deason, A. J. 2018, MNRAS, 478, 611
Bensby, T., Feltzing, S., & Oey, M. S. 2014, A&A, 562, A71
Bergemann, M. & Cescutti, G. 2010, A&A, 522, A9
Bergemann, M., Collet, R., Schönrich, R., et al. 2017, ApJ, 847, 16
Bergemann, M., Gallagher, A. J., Eitner, P., et al. 2019, A&A, 631, A80
Bonifacio, P., Monaco, L., Salvadori, S., et al. 2021a, A&A, 651, A79
Bonifacio, P., Monaco, L., Salvadori, S., et al. 2021b, A&A, 651, A79
Bouchy, F. & Sophie Team. 2006, in Tenth Anniversary of 51 Peg-b: Status of and prospects for hot Jupiter studies, ed. L. Arnold, F. Bouchy, & C. Moutou, 319–325
Bovy, J. 2015, ApJS, 216, 29
Bovy, J., Allende Prieto, C., Beers, T. C., et al. 2012, ApJ, 759, 131
Bressan, A., Marigo, P., Girardi, L., et al. 2012, MNRAS, 427, 127
Burbidge, E. M., Burbidge, G. R., Fowler, W. A., & Hoyle, F. 1957, Rev. Mod. Phys., 29, 547
Caffau, E., Bonifacio, P., François, P., et al. 2011, Nature, 477, 67
Caffau, E., Ludwig, H. G., Steffen, M., et al. 2008, A&A, 488, 1031
Caffau, E., Monaco, L., Spite, M., et al. 2014, A&A, 568, A29
Cayrel, R., Depagne, E., Spite, M., et al. 2004, A&A, 416, 1117
Cescutti, G. & Kobayashi, C. 2017, A&A, 607, A23
Cescutti, G., Matteucci, F., François, P., & Chiappini, C. 2007, A&A, 462, 943
Cescutti, G., Matteucci, F., Lanfranchi, G. A., & McWilliam, A. 2008, A&A, 491, 401
Cescutti, G., Molaro, P., & Fu, X. 2020, Mem. Soc. Astron. Italiana, 91, 153
Chiappini, C., Matteucci, F., & Gratton, R. 1997, ApJ, 477, 765
Cosentino, R., Lovis, C., Pepe, F., et al. 2012, in Society of Photo-Optical Instrumentation Engineers (SPIE) Conference Series, Vol. 8446, Ground-based and Airborne Instrumentation for Astronomy IV, ed. I. S. McLean, S. K. Ramsay, & H. Takami, 84461V
Donati, J. F., Catala, C., Landstreet, J. D., & Petit, P. 2006, in Astronomical Society of the Pacific Conference Series, Vol. 358, Solar Polarization 4, ed. R. Casini & B. W. Lites, 362
Donati, J. F., Semel, M., Carter, B. D., Rees, D. E., & Collier Cameron, A. 1997, MNRAS, 291, 658
Eisenstein, D. J., Weinberg, D. H., Agol, E., et al. 2011, AJ, 142, 72
Eitner, P., Bergemann, M., Hansen, C. J., et al. 2020, A&A, 635, A38
Feuillet, D. K., Sahlholdt, C. L., Feltzing, S., & Casagrande, L. 2021, MNRAS, 508, 1489
François, P., Matteucci, F., Cayrel, R., et al. 2004, A&A, 421, 613
Fuhrmann, K., Chini, R., Kaderhandt, L., & Chen, Z. 2017, MNRAS, 464, 2610
Hansen, C. J., Koch, A., Mashonkina, L., et al. 2020, A&A, 643, A49
Haywood, M., Di Matteo, P., Lehnert, M. D., et al. 2018, ApJ, 863, 113
Helmi, A., Babusiaux, C., Koppelman, H. H., et al. 2018, Nature, 563, 85
Ishigaki, M. N., Aoki, W., & Chiba, M. 2013, ApJ, 771, 67
Ishigaki, M. N., Chiba, M., & Aoki, W. 2012, ApJ, 753, 64
Kobayashi, C., Karakas, A. I., & Umeda, H. 2011, MNRAS, 414, 3231
Kurucz, R. 1993a, ATLAS9 Stellar Atmosphere Programs and 2 km/s grid. Kurucz CD-ROM No. 13. Cambridge, 13
Kurucz, R. L. 1993b, SYNTHE spectrum synthesis programs and line data
Kurucz, R. L. 2005, Memorie della Societa Astronomica Italiana Supplementi, 8, 14
Lanfranchi, G. A., Matteucci, F., & Cescutti, G. 2008, A&A, 481, 635
Limongi, M. & Chieffi, A. 2018, ApJS, 237, 13
Lind, K., Bergemann, M., & Asplund, M. 2012, MNRAS, 427, 50
Lindegren, L., Bastian, U., Biermann, M., et al. 2021, A&A, 649, A4
Lodders, K., Palme, H., & Gail, H. P. 2009, Landolt Börnstein, 4B, 712
Marigo, P., Girardi, L., Bressan, A., et al. 2017, ApJ, 835, 77
Mashonkina, L. 2020, MNRAS, 493, 6095
Mashonkina, L., Jablonka, P., Sitnova, T., Pakhomov, Y., & North, P. 2017, A&A, 608, A89
Matas Pinto, A. d. M., Caffau, E., François, P., et al. ????, Astronomische Nachrichten, n/a [https://onlinelibrary.wiley.com/doi/pdf/10.1002/asna.20210032]
Mott, A., Spitoni, E., & Matteucci, F. 2013, MNRAS, 435, 2918
Mucciarelli, A., Pancino, E., Lovisi, L., Ferraro, F. R., & Lapenna, E. 2013, GALA: Stellar atmospheric parameters and chemical abundances
Myeong, G. C., Vasiliev, E., Iorio, G., Evans, N. W., & Belokurov, V. 2019, MNRAS, 488, 1235
Palla, M., Matteucci, F., Spitoni, E., Vincenzo, F., & Grisoni, V. 2020, MNRAS, 498, 1710
Reggiani, H., Amarsi, A. M., Lind, K., et al. 2019, A&A, 627, A177
Roederer, I. U., Preston, G. W., Thompson, I. B., et al. 2014, AJ, 147, 136
Romano, D., Karakas, A. I., Tosi, M., & Matteucci, F. 2010, A&A, 522, A32
Sbordone, L., Caffau, E., Bonifacio, P., & Duffau, S. 2014, A&A, 564, A109
Scalo, J. M. 1986, Fund. Cosmic Phys., 11, 1
Schlafly, E. F., Finkbeiner, D. P., Jurić, M., et al. 2012, ApJ, 756, 158
Schönrich, R., Binney, J., & Dehnen, W. 2010, MNRAS, 403, 1829
Seitenzahl, I. R., Cescutti, G., Röpke, F. K., Ruiter, A. J., & Pakmor, R. 2013, A&A, 559, L5
Sitnova, T. M., Mashonkina, L. I., & Ryabchikova, T. A. 2016, MNRAS, 461, 1000
Spitoni, E., Cescutti, G., Minchev, I., et al. 2019a, A&A, 628, A38
Spitoni, E., Romano, D., Matteucci, F., & Ciotti, L. 2015, ApJ, 802, 129
Spitoni, E., Silva Aguirre, V., Matteucci, F., Calura, F., & Grisoni, V. 2019b, A&A, 623, A60
Spitoni, E., Verma, K., Silva Aguirre, V., & Calura, F. 2020, A&A, 635, A58
Spitoni, E., Verma, K., Silva Aguirre, V., et al. 2021, A&A, 647, A73
Steffen, M., Prakapavičius, D., Caffau, E., et al. 2015, A&A, 583, A57
Takeda, Y., Hashimoto, O., Taguchi, H., et al. 2005, PASJ, 57, 751
Telting, J. H., Avila, G., Buchhave, L., et al. 2014, Astronomische Nachrichten, 335, 41
Timmes, F. X., Woosley, S. E., & Weaver, T. A. 1995, ApJS, 98, 617
Villanova, S., Monaco, L., Geisler, D., et al. 2019, ApJ, 882, 174
Wright, J. T. & Eastman, J. D. 2014, PASP, 126, 838
Yong, D., Alves Brito, A., Da Costa, G. S., et al. 2014, MNRAS, 439, 2638

Appendix A: Tables with Chemical abundances

Table A.1. Table with the abundances of elements in their ionization state from O I to Sc II in [X/H], with the sigma based on the line to line dispersion and the number of lines for each ion.

Star	S/N@550 nm	O I	σ	N	Na I	σ	N	Mg I	σ	N	Al I	σ	N	Si I	σ	N	Ca I	σ	N	Sc II	σ	N
BD-00 4538	> 100	-1.123	0.0	1	-2.107	0.048	3	-1.422	0.114	4	-99.0	0.0	0	-1.519	0.046	14	-1.551	0.057	25	-1.536	0.116	10
BD+03 4904	72	-1.432	0.0	1	-99.0	0.0	0	-2.028	0.085	4	-99.0	0.0	0	-2.226	0.0	1	-2.251	0.073	21	-2.246	0.148	8
BD+04 18	71	-0.594	0.0	1	-1.795	0.033	2	-0.898	0.0	1	-1.438	0.027	2	-1.094	0.094	11	-1.277	0.055	12	-1.04	0.104	4
BD+07 4625	> 100	-99.0	0.0	0	-2.359	0.005	2	-1.577	0.072	4	-99.0	0.0	0	-1.745	0.082	12	-1.683	0.046	26	-1.712	0.165	11
BD+07 4625	93	-99.0	0.0	0	-2.376	0.02	3	-1.628	0.089	3	-99.0	0.0	0	-1.725	0.073	11	-1.731	0.05	18	-1.783	0.091	8
BD+11 2896	97	-0.804	0.0	1	-1.579	0.046	4	-0.999	0.075	3	-1.323	0.024	3	-1.113	0.1	19	-1.093	0.063	19	-1.071	0.075	5
BD+20 3298	99	-1.08	0.0	1	-2.065	0.036	4	-1.437	0.054	3	-1.852	0.0	1	-1.534	0.092	20	-1.566	0.053	23	-1.626	0.115	8
BD+21 4579	75	-99.0	0.0	0	-99.0	0.0	0	-1.922	0.104	3	-99.0	0.0	0	-1.99	0.0	1	-2.154	0.088	20	-2.039	0.099	7
BD+25 4520	85	-1.448	0.064	2	-2.505	0.046	2	-1.783	0.0	1	-99.0	0.0	0	-1.935	0.079	11	-1.969	0.061	20	-1.935	0.128	8
BD+31 2143	> 100	-1.274	0.034	2	-2.495	0.024	2	-1.728	0.144	5	-99.0	0.0	0	-1.806	0.089	10	-1.955	0.065	27	-1.955	0.127	10
BD+32 2483	> 100	-99.0	0.0	0	-2.441	0.053	3	-1.674	0.109	4	-99.0	0.0	0	-1.768	0.067	12	-1.867	0.056	26	-1.918	0.104	11
BD+35 4847	94	-1.037	0.091	2	-1.831	0.041	4	-1.271	0.0	1	-1.458	0.044	2	-1.297	0.07	17	-1.508	0.04	18	-1.395	0.113	7
BD+39 3309	98	-99.0	0.0	0	-99.0	0.0	0	-2.115	0.072	3	-99.0	0.0	0	-2.108	0.037	2	-2.222	0.1	24	-2.321	0.137	9
BD+48 2167	99	-1.23	0.054	2	-2.405	0.03	3	-1.632	0.132	3	-99.0	0.0	0	-1.83	0.083	9	-1.909	0.066	23	-1.896	0.108	10
BD-07 3523	99	-1.214	0.0	1	-2.088	0.029	4	-1.42	0.0	1	-1.896	0.0	1	-1.623	0.084	17	-1.62	0.042	21	-1.55	0.135	7
BD+06 2880	98	-0.617	0.039	2	-1.694	0.057	4	-0.923	0.0	1	-1.423	0.006	2	-1.128	0.086	17	-1.216	0.052	14	-1.149	0.133	5
BD+25 4520	94	-1.532	0.036	2	-2.489	0.014	3	-1.703	0.148	2	-99.0	0.0	0	-1.933	0.039	13	-1.957	0.04	23	-1.979	0.134	11
HD 115575	99	-1.176	0.016	2	-2.312	0.054	3	-1.517	0.028	2	-1.92	0.0	1	-1.668	0.063	16	-1.661	0.052	25	-1.633	0.136	10
HD 139423	97	-1.003	0.013	2	-1.821	0.031	4	-1.151	0.0	1	-1.532	0.062	2	-1.372	0.046	16	-1.31	0.047	22	-1.482	0.115	9
HD 142614	94	-0.856	0.022	2	-1.513	0.038	4	-0.942	0.0	1	-1.318	0.01	2	-1.123	0.078	15	-1.086	0.052	16	-1.086	0.1	6
HD 208316	97	-0.821	0.016	2	-1.652	0.044	4	-1.006	0.0	1	-1.433	0.009	2	-1.229	0.046	14	-1.19	0.049	18	-1.195	0.125	6
HD 238439	99	-1.216	0.0	1	-2.259	0.023	4	-1.507	0.0	1	-1.981	0.0	1	-1.752	0.071	15	-1.715	0.047	22	-1.754	0.099	7
HD 354750	52	-99.0	0.0	0	-2.214	0.0	1	-1.814	0.075	4	-99.0	0.0	0	-1.768	0.137	2	-1.943	0.08	18	-2.16	0.144	8
TYC 1008-120	67	-1.367	0.0	1	-2.377	0.008	2	-1.659	0.0	1	-99.0	0.0	0	-1.727	0.154	12	-1.841	0.058	19	-1.716	0.122	7
TYC 2588 138	65	-1.383	0.0	1	-1.397	0.08	4	-1.204	0.229	2	-1.112	0.034	3	-1.341	0.129	18	-1.386	0.08	20	-1.333	0.134	8
TYC 2824-196	70	-0.839	0.036	2	-1.823	0.047	4	-1.087	0.0	1	-1.458	0.0	1	-1.216	0.142	15	-1.283	0.083	16	-1.191	0.119	5
TYC 3085 119	97	-0.772	0.0	1	-1.557	0.071	4	-1.02	0.164	4	-1.189	0.056	2	-1.023	0.051	16	-1.084	0.057	24	-1.022	0.095	9
TYC 33-446	69	-1.065	0.0	1	-2.292	0.228	3	-1.694	0.051	2	-99.0	0.0	0	-1.762	0.118	11	-1.851	0.06	24	-1.849	0.154	10
TYC 3944-698	69	-1.23	0.0	1	-2.297	0.106	4	-1.639	0.0	1	-99.0	0.0	0	-1.706	0.134	10	-1.835	0.084	12	-1.723	0.148	5
TYC 4001-116	84	-0.592	0.026	2	-1.775	0.047	3	-1.084	0.0	1	-1.619	0.081	2	-1.208	0.091	12	-1.423	0.076	17	-1.301	0.136	4
TYC 4221-640	67	-1.407	0.0	1	-2.538	0.111	2	-1.866	0.069	3	-99.0	0.0	0	-2.117	0.067	2	-2.084	0.061	20	-2.094	0.098	7
TYC 4267-202	87	-0.993	0.0	1	-1.894	0.038	4	-1.222	0.0	1	-1.739	0.0	1	-1.523	0.044	12	-1.399	0.076	20	-1.66	0.111	8
TYC 4331-136	67	-99.0	0.0	0	-2.745	0.0	1	-1.927	0.019	2	-99.0	0.0	0	-1.964	0.112	4	-2.233	0.076	22	-2.004	0.145	6
TYC 4-369-1	50	-0.879	0.0	1	-1.974	0.078	4	-1.312	0.0	1	-1.696	0.0	1	-1.454	0.106	15	-1.536	0.061	21	-1.363	0.136	6
TYC 4584-784	49	-1.32	0.0	1	-2.124	0.057	3	-1.519	0.0	1	-1.64	0.0	1	-1.571	0.083	10	-1.68	0.066	20	-1.659	0.118	9

Table A.2. Table with the abundances of elements in their ionization state from Ti I to Fe I in [X/H], with the sigma based on the line to line dispersion and the number of lines for each ion.

Star	Ti I	σ	N	Ti II	σ	N	V I	σ	N	Cr I	σ	N	Cr II	σ	N	Mn I	σ	N	Fe I	σ	N
BD-00 4538	-1.634	0.074	52	-1.473	0.119	28	-1.958	0.099	20	-1.935	0.093	23	-1.771	0.098	7	-2.2	0.069	14	-1.9	0.094	276
BD+03 4904	-2.282	0.102	31	-2.166	0.153	28	-2.595	0.115	6	-2.686	0.111	14	-2.472	0.11	6	-2.912	0.032	7	-2.573	0.122	175
BD+04 18	-1.265	0.096	22	-1.047	0.082	10	-1.618	0.107	11	-1.655	0.153	7	-1.231	0.0	1	-1.845	0.113	9	-1.48	0.123	139
BD+07 4625	-1.744	0.083	47	-1.624	0.09	28	-2.037	0.096	10	-2.01	0.087	20	-1.963	0.087	7	-2.265	0.061	13	-1.926	0.102	270
BD+07 4625	-1.724	0.066	37	-1.67	0.077	21	-2.022	0.059	7	-2.054	0.054	15	-1.931	0.057	5	-2.323	0.05	12	-1.953	0.11	229
BD+11 2896	-1.148	0.072	48	-1.012	0.101	21	-1.441	0.086	18	-1.425	0.133	16	-1.348	0.121	5	-1.649	0.078	10	-1.413	0.12	219
BD+20 3298	-1.621	0.069	52	-1.515	0.073	23	-1.993	0.07	19	-1.942	0.088	17	-1.851	0.041	3	-2.277	0.086	13	-1.952	0.096	245
BD+21 4579	-2.217	0.141	32	-1.98	0.144	24	-2.651	0.129	4	-2.7	0.106	12	-2.394	0.143	7	-2.942	0.098	7	-2.504	0.137	179
BD+25 4520	-2.035	0.076	46	-1.953	0.09	16	-2.374	0.056	13	-2.388	0.073	13	-2.31	0.092	6	-2.596	0.072	14	-2.277	0.096	207
BD+25 4520	-2.046	0.057	51	-1.906	0.095	24	-2.381	0.051	18	-2.383	0.055	17	-2.269	0.077	7	-2.614	0.106	14	-2.271	0.093	267
BD+31 2143	-2.044	0.055	41	-1.891	0.117	30	-2.388	0.072	9	-2.454	0.067	20	-2.342	0.08	6	-2.761	0.098	12	-2.361	0.101	234
BD+32 2483	-1.93	0.059	45	-1.814	0.112	30	-2.291	0.069	11	-2.317	0.082	19	-2.227	0.075	7	-2.622	0.095	13	-2.245	0.105	255
BD+35 4847	-1.534	0.101	54	-1.467	0.117	28	-1.912	0.059	19	-1.916	0.083	19	-1.794	0.144	7	-2.146	0.063	13	-1.907	0.099	239
BD+39 3309	-2.149	0.085	27	-2.025	0.123	23	-2.428	0.0	1	-2.71	0.057	11	-2.417	0.104	4	-2.776	0.012	6	-2.584	0.131	191
BD+48 2167	-1.955	0.074	48	-1.794	0.107	24	-2.378	0.058	8	-2.371	0.082	20	-2.235	0.088	7	-2.719	0.092	13	-2.279	0.107	238
BD-07 3523	-1.612	0.078	49	-1.511	0.076	21	-1.952	0.065	18	-1.979	0.078	15	-1.857	0.029	4	-2.236	0.083	15	-1.951	0.103	229
BD+06 2880	-1.231	0.081	33	-1.034	0.06	16	-1.539	0.052	15	-1.558	0.102	8	-1.411	0.113	5	-1.801	0.101	11	-1.448	0.105	175
HD 115575	-1.68	0.08	54	-1.542	0.11	22	-2.011	0.066	19	-2.037	0.076	16	-1.935	0.104	6	-2.273	0.052	14	-1.993	0.091	248
HD 139423	-1.329	0.082	50	-1.391	0.122	26	-1.651	0.06	18	-1.703	0.097	16	-1.714	0.099	5	-1.926	0.06	12	-1.703	0.109	230
HD 142614	-1.119	0.07	42	-1.079	0.077	15	-1.416	0.073	14	-1.503	0.138	12	-1.389	0.015	2	-1.708	0.1	11	-1.454	0.107	197
HD 208316	-1.225	0.066	40	-1.177	0.059	19	-1.537	0.084	16	-1.634	0.094	15	-1.647	0.126	3	-1.851	0.064	9	-1.606	0.101	217
HD 238439	-1.705	0.081	44	-1.654	0.081	15	-2.094	0.072	19	-2.13	0.065	16	-2.073	0.127	7	-2.386	0.07	14	-2.09	0.113	251
HD 354750	-1.999	0.075	26	-2.005	0.125	29	-2.268	0.126	3	-2.41	0.129	15	-2.45	0.194	5	-2.71	0.111	7	-2.352	0.11	176
TYC 1008-120	-1.929	0.075	43	-1.696	0.148	25	-2.271	0.064	14	-2.305	0.092	15	-2.076	0.133	6	-2.568	0.103	12	-2.229	0.098	204
TYC 2588 138	-1.397	0.082	50	-1.318	0.103	24	-1.697	0.082	20	-1.752	0.154	21	-1.653	0.162	7	-1.985	0.098	11	-1.733	0.122	235
TYC 2824-196	-1.289	0.079	27	-1.184	0.151	17	-1.605	0.099	13	-1.637	0.137	9	-1.427	0.189	3	-1.907	0.111	8	-1.6	0.137	169
TYC 3085 119	-1.158	0.076	56	-1.008	0.07	24	-1.495	0.074	18	-1.503	0.07	19	-1.353	0.048	6	-1.778	0.04	12	-1.509	0.102	276
TYC 33-446	-1.886	0.069	41	-1.79	0.092	24	-2.225	0.101	16	-2.311	0.08	16	-2.179	0.122	7	-2.513	0.065	13	-2.215	0.117	204
TYC 3944-698	-1.716	0.114	32	-1.535	0.105	17	-2.061	0.084	17	-2.076	0.083	9	-1.959	0.128	5	-2.367	0.076	11	-2.181	0.128	141
TYC 4001-116	-1.501	0.068	34	-1.131	0.096	15	-1.856	0.069	14	-1.843	0.085	11	-1.523	0.098	4	-2.025	0.107	11	-1.619	0.106	164
TYC 4221-640	-2.189	0.075	42	-2.086	0.104	23	-2.413	0.11	10	-2.42	0.088	14	-2.286	0.062	5	-2.503	0.075	11	-2.267	0.105	217
TYC 4267-202	-1.222	0.129	45	-1.566	0.147	15	-1.518	0.052	19	-1.736	0.091	13	-2.142	0.125	6	-1.938	0.091	13	-1.737	0.14	209
TYC 4331-136	-2.291	0.116	39	-2.066	0.108	28	-2.602	0.126	15	-2.666	0.085	15	-2.373	0.147	6	-2.811	0.116	13	-2.531	0.108	188
TYC 4-369-1	-1.608	0.083	45	-1.352	0.108	26	-1.936	0.067	17	-1.965	0.103	17	-1.715	0.111	6	-2.134	0.082	13	-1.836	0.107	198
TYC 4584-784	-1.754	0.135	46	-1.572	0.169	30	-2.07	0.136	16	-2.106	0.112	19	-1.903	0.114	7	-2.334	0.09	14	-2.033	0.113	228

Table A.3. Table with the abundances of elements in their ionization state from Fe II I to Zn I in [X/H], with the sigma based on the line to line dispersion and the number of lines for each ion.

Star	Fe II	σ	N	Co I	σ	N	Ni I	σ	N	Cu I	σ	N	Zn I	σ	N
BD-00 4538	-1.75	0.142	26	-1.893	0.092	19	-1.952	0.1	64	-2.467	0.149	4	-1.865	0.031	2
BD+03 4904	-2.466	0.174	20	-2.472	0.093	6	-2.567	0.12	35	-3.132	0.0	1	-2.331	0.045	2
BD+04 18	-1.284	0.308	13	-1.445	0.13	12	-1.566	0.157	40	-1.927	0.105	2	–	0.0	0
BD+07 4625	-1.917	0.13	31	-1.929	0.104	12	-1.994	0.114	61	-2.705	0.0	1	-2.037	0.051	2
BD+07 4625	-1.886	0.101	21	-1.934	0.136	12	-2.041	0.116	48	-2.707	0.0	1	-2.074	0.029	2
BD+11 2896	-1.299	0.199	20	-1.355	0.153	17	-1.469	0.132	64	-1.877	0.107	3	-1.464	0.043	2
BD+20 3298	-1.864	0.165	20	-1.887	0.09	19	-2.013	0.134	64	-2.435	0.101	3	-2.007	0.005	2
BD+21 4579	-2.343	0.122	17	-2.413	0.023	5	-2.513	0.132	34	–	0.0	0	-2.352	0.056	2
BD+25 4520	-2.128	0.172	18	-2.211	0.143	16	-2.321	0.119	48	-2.695	0.234	4	-2.367	0.015	2
BD+25 4520	-2.103	0.114	18	-2.208	0.135	17	-2.32	0.112	61	-2.839	0.118	4	-2.306	0.049	2
BD+31 2143	-2.239	0.116	25	-2.337	0.066	7	-2.351	0.105	55	-2.918	0.0	1	-2.211	0.027	2
BD+32 2483	-2.197	0.162	29	-2.179	0.132	12	-2.248	0.13	59	-2.856	0.07	2	-2.167	0.059	2
BD+35 4847	-1.903	0.171	26	-1.788	0.111	19	-1.924	0.13	64	-2.135	0.141	4	-1.872	0.022	2
BD+39 3309	-2.455	0.126	23	-2.409	0.051	2	-2.433	0.084	36	–	0.0	0	-2.144	0.047	2
BD+48 2167	-2.15	0.123	24	-2.206	0.141	13	-2.335	0.126	57	-2.868	0.05	2	-2.195	0.012	2
BD-07 3523	-1.871	0.162	18	-1.858	0.11	14	-2.021	0.148	61	-2.434	0.098	3	-2.093	0.06	2
BD+06 2880	-1.3	0.226	17	-1.415	0.134	14	-1.534	0.135	46	-1.98	0.13	3	-1.47	0.042	2
HD 115575	-1.859	0.122	19	-1.895	0.092	15	-2.016	0.117	62	-2.523	0.101	4	-1.934	0.011	2
HD 139423	-1.784	0.149	18	-1.592	0.13	15	-1.771	0.116	58	-2.147	0.122	3	-1.823	0.059	2
HD 142614	-1.474	0.175	18	-1.337	0.105	14	-1.504	0.125	53	-1.868	0.11	3	-1.575	0.029	2
HD 208316	-1.569	0.101	17	-1.469	0.145	15	-1.653	0.124	52	-1.968	0.109	3	-1.628	0.0	2
HD 238439	-2.019	0.13	18	-2.012	0.14	15	-2.174	0.14	61	-2.57	0.14	3	-2.174	0.037	2
HD 354750	-2.417	0.142	20	-2.284	0.106	4	-2.339	0.106	28	-2.994	0.0	1	-2.256	0.089	2
TYC 1008-120	-1.998	0.17	16	-2.174	0.133	14	-2.278	0.115	44	-2.78	0.034	2	-2.239	0.047	2
TYC 2588 138	-1.701	0.204	23	-1.58	0.132	18	-1.757	0.172	63	-2.205	0.071	3	-1.785	0.197	2
TYC 2824-196	-1.445	0.383	16	-1.537	0.134	14	-1.687	0.138	43	-2.086	0.124	3	-1.673	0.029	2
TYC 3085 119	-1.424	0.172	23	-1.417	0.117	18	-1.481	0.111	66	-1.83	0.084	4	-1.351	0.084	2
TYC 33-446	-2.204	0.204	22	-2.068	0.097	12	-2.226	0.139	49	-2.64	0.172	3	-2.305	0.003	2
TYC 3944-698	-2.055	0.205	18	-2.04	0.167	12	-2.169	0.15	37	-2.638	0.024	2	-1.593	0.018	2
TYC 4001-116	-1.283	0.286	15	-1.628	0.11	13	-1.679	0.132	46	-2.132	0.14	4	-1.492	0.104	2
TYC 4221-640	-2.189	0.219	19	-2.165	0.128	11	-2.286	0.132	43	-2.797	0.029	3	-2.253	0.038	2
TYC 4267-202	-2.083	0.155	17	-1.483	0.158	16	-1.762	0.193	50	-2.006	0.024	2	-2.082	0.025	2
TYC 4331-136	-2.43	0.229	22	-2.416	0.115	10	-2.502	0.127	46	-3.178	0.197	2	-2.265	0.024	2
TYC 4-369-1	-1.663	0.245	21	-1.815	0.107	16	-1.896	0.131	49	-2.409	0.045	3	-1.81	0.148	2
TYC 4584-784	-1.854	0.246	22	-1.936	0.124	15	-2.057	0.117	53	-2.58	0.138	4	-2.07	0.163	2

Table A.4. Log of the observations and radial velocities for the stars observed with HARPS-N

Star	alpha2000 J2000	delta2000 J2000	BJD days	Date	t_{exp} s	RV km s^{-1}	σ_{RV} km s^{-1}
HD 87740	10:07:10.25	+03:41:23.3	2458980.40412383	2020-05-10	3000	–23.9993	0.0016
HD 91276	10:32:57.37	+35:22:56.6	2458980.44256365	2020-05-10	3000	+23.9350	0.0017
BD +13 2383	11:17:37.07	+12:24:10.0	2458980.48078609	2020-05-10	2400	–11.5311	0.0023
BD +41 2520	14:42:02.54	+41:14:11.6	2458980.60643665	2020-05-11	3600	+11.6820	0.0014
HD 130971	14:51:15.68	–08:59:01.8	2458980.56913504	2020-05-11	3600	+23.7756	0.0012
BD +24 2817	15:05:56.81	+24:05:51.7	2458980.65155434	2020-05-11	3000	–43.1845	0.0009
HD 138934	15:34:21.37	+23:12:36.6	2458980.68241001	2020-05-11	2100	+18.3412	0.0007
HD 143348	15:58:36.55	+34:11:33.4	2458980.70923832	2020-05-11	2400	–73.7397	0.0012
BD –07 3523	13:00:33.60	–07:59:38.2	2459010.45002716	2020-06-09	3600	+73.5710	0.0025
HD 115575	13:18:09.97	–13:58:45.8	2459010.40738054	2020-06-09	3600	+188.4806	0.0029
BD +06 2880	14:25:10.31	+06:07:14.9	2459010.49153284	2020-06-09	3000	+37.3641	0.0021
HD 238439	15:17:00.58	+54:35:38.6	2459010.53202863	2020-06-10	3600	–65.0949	0.0024
HD 139423	15:37:45.83	+11:36:11.6	2459010.56447555	2020-06-10	1200	+183.3917	0.0023
HD 142614	15:55:15.38	+08:13:27.8	2459010.58578868	2020-06-10	2100	-337.1939	0.0019
BD +254520	21:22:08.32	+25:45:15.8	2459010.61970877	2020-06-10	3600	+22.8268	0.0025
HD 208316	21:55:36.03	–04:13:27.4	2459010.65672317	2020-06-10	2100	–146.1986	0.0019

Table A.5. Log of the observations and radial velocities for the stars observed with FIES

STAR	α J2000	δ J2000	BJD days	Date	t_{exp} s	RV km s^{-1}	σ_{RV} km s^{-1}
BD +07 4625	21:07:13.10	+07:44:19.8	2459032.670574271	2020-07-02	2200	–494.883	0.004
	21:07:13.10	+07:44:19.8	2459032.696585007	2020-07-02	2200	–494.551	0.003
BD +35 4847	22:37:13.45	+36:08:21.6	2459033.675984722	2020-07-03	2800	–139.739	0.003
	22:37:13.45	+36:08:21.6	2459033.708940891	2020-07-03	2800	–139.742	0.003
BD +11 2896	16:01:04.87	+11:12:56.2	2459001.539097893	2020-06-01	3000	–218.821	0.002
	16:01:04.87	+11:12:56.2	2459001.574364527	2020-06-01	3000	–218.831	0.002
HD 165400	18:05:30.45	+09:49:30.4	2459000.690305141	2020-05-31	2800	–2.745	0.002
BD –00 3963	20:17:12.53	+00:21:22.7	2459036.622693848	2020-07-06	2200	–42.165	0.002
	20:17:12.53	+00:21:22.7	2459036.648704157	2020-07-06	2200	–42.159	0.002
BD –00 4538	23:38:18.78	+00:46:51.5	2459069.603750275	2020-08-08	2900	–190.753	0.003
	23:38:18.78	+00:46:51.5	2459069.637862387	2020-08-08	2900	–191.027	0.003

Table A.6. Log of the observations and radial velocities for the stars observed with Sophie

STAR	α	δ	BJD	Date	t_{exp}	RV	σ_{RV}
	J2000	J2000	days		s	km s^{-1}	km s^{-1}
TYC 4-369-1	00:08:36.02	+02:58:01.7	2459087.56089588	2020-08-25	3600	+3.982	0.006
BD +04 18	00:12:49.90	+05:37:39.3	2459086.6077017	2020-08-25	3600	–29.987	0.002
TYC 33-446-1	01:54:22.17	+03:41:45.3	2459087.64126008	2020-08-26	3491	–99.892	0.004
TYC 2824-1963-1	01:58:38.93	+41:46:30.4	2459086.6437657	2020-08-25	2618	+52.907	0.003
	01:58:38.93	+41:46:30.4	2459087.5992952	2020-08-26	3105	+52.816	0.002
TYC 4331-136-1	03:57:14.19	+69:44:45.1	2459088.63728359	2020-08-27	3600	–110.967	0.005
TYC 1008-1200-1	18:06:31.58	+08:44:54.7	2459086.3381710	2020-08-24	3600	–393.813	0.007
	18:06:31.58	+08:44:54.7	2459087.3363853	2020-08-25	3600	–393.838	0.005
TYC 2113-471-1	18:56:41.55	+25:16:50.8	2459087.38188494	2020-08-25	3600	–252.760	0.004
	18:56:41.55	+25:16:50.8	2459088.32588031	2020-08-26	3600	–252.858	0.004
TYC 4221-640-1	19:09:19.27	+63:03:44.2	2459086.38173932	2020-08-24	3600		
	19:09:19.27	+63:03:44.2	2459088.36663955	2020-08-26	3600	–277.441	0.006
TYC 4584-784-1	19:22:56.40	+76:32:43.3	2459088.41633999	2020-08-26	3600	–295.607	0.004
TYC 3944-698-1	20:02:59.61	+58:01:07.1	2459086.4263490	2020-08-24	3600	–255.266	0.004
HD 354750	20:04:29.05	+13:35:31.0	2459088.46611671	2020-08-26	3600	–168.281	0.008
BD +25 4520	21:22:08.32	+25:45:15.8	2459087.42848911	2020-08-25	3600	+23.518	0.003
TYC 4267-2023-1	22:01:46.08	+62:27:40.6	2459086.4710943	2020-08-24	3600	–346.268	0.003
TYC 565-1564-1	22:10:38.77	+05:16:14.6	2459087.47351081	2020-08-25	3600	–175.181	0.003
BD +21 4759	22:28:46.35	+22:09:11.4	2459088.59697759	2020-08-27	3600	–202.045	0.006
TYC 2228-838-1	22:38:23.28	+27:34:24.7	2459088.5536172	2020-08-27	3600	–145.006	0.002
TYC 4001-1161-1	23:47:30.68	+53:47:16.5	2459086.5158160	2020-08-24	3600	-397.649	0.003
	23:47:30.68	+53:47:16.5	2459087.5143166	2020-08-25	3506	-397.617	0.003
BD +03 4904	23:55:28.37	+04:21:17.9	2459086.5634472	2020-08-25	3600	–208.370	0.006
BD +07 4625	21:07:13.10	+07:44:19.7	2459088.51050063	2020-08-27	3600	–495.699	0.002

Table A.7. Log of the observations and radial velocities for the stars observed with ESPaDOnS

STAR	α	δ	BJD	Date	t_{exp}	RV	σ_{RV}
	J2000	J2000	days		s	km s^{-1}	km s^{-1}
BD+20 3298	16:36:33.15	+20:25:46.1	2459016.033335	2020-06-15	2380	–257.104	0.003
BD+31 2143	10:28:17.23	+30:26:29.2	2459180.153748	2020-11-26	2380	+64.157	0.004
BD+48 2167	13:59:19.74	+48:05:35.5	2459189.153872	2020-12-05	2380	–108.203	0.003
BD+39 3309	18:03:47.35	+39:32:31.3	2459016.091233	2020-06-15	2380	–249.092	0.005
BD+32 2483	14:31:38.96	+31:58:58.4	2459012.887960	2020-06-12	2380	+4.145	0.003
TYC 3085-119-1	17:16:36.98	+44:10:43.4	2458739.761057	2019-09-13	2380	–106.234	0.003
	17:16:36.98	+44:10:43.4	2458739.790407	2019-09-13	2380	–105.941	0.003
TYC 2588-1386-1	16:41:32.08	+36:24:42.6	2458739.725085	2019-09-13	2380	–249.674	0.003